

Automated Multi-Material Additive Manufacturing: An Initial Exploration with Concrete

William T. Makinen

April 18th, 2022



Submitted in partial fulfillment
of the requirements for the degree of
Bachelor of Science in Engineering
Department of Electrical and Computer Engineering
Princeton University

I hereby declare that this Independent Work report represents my own work in accordance with University regulations.

A handwritten signature in black ink, appearing to read "William T. Makinen".

William T. Makinen

Automated Multi-Material Additive Manufacturing: An Initial Exploration with Concrete

William Makinen

Abstract

Additive manufacturing of concrete has seen an increase of interest in recent years given its potential to revolutionize the construction industry by circumventing the geometric constraints of traditional fabrication techniques while achieving improved mechanical properties and reducing construction time and cost. A well-known limitation of the material is its weak tensile strength, often requiring concrete structures to be reinforced in order to meet design standards. However, most concrete 3D-printing research to date has focused on single-material systems that do little to augment the material's mechanical properties. This work represents an initial attempt to address these concerns by detailing the development of a desktop-scale multi-material cement paste 3D-printer that combines cement paste (without aggregates) with other materials in situ to the printing process to form cementitious multi-materials. This was achieved by building a tool-changing 3D-printer that is capable of switching between different print heads and materials by following toolpaths generated with a software workflow that only needs high-level parametric inputs from the user. This device was then used to develop several multi-material architectures which were tested in bending according to ASTM standards. They showed improved overall toughness, modulus of rupture, and fracture toughness compared to cast and single-material 3D-printed cement paste components, validating multi-material cement 3D-printing as a viable way to fabricate cementitious components with improved mechanical properties.

ACKNOWLEDGEMENTS

I must first thank my advisor Professor Reza Moini, who was willing to let an electrical engineer with absolutely no knowledge of civil engineering to run with this project, even when I didn't really know what I was doing or talking about most of the time.

I must also thank the other members of the lab, Arjun, Hadi, and especially Shashank, who made many late nights covered in concrete trying to get prints to work a bit more enjoyable.

A very heartfelt thanks must also go out to the late Sanjay of E3D. Sanjay was one of the most passionate people I have ever met, and whenever he stopped by my desk during my internship last summer it was a pure joy talking to him, whether it was about this thesis project or insulin pumps. He also graciously provided me with an E3D ToolChanger at cost, which was a huge help in getting this project off the ground. I haven't experienced much loss in my life, however finding out about Sanjay's passing affected me much more than expected, and I will never forget him. A quick thanks to the E3D family as a whole as well: Rory, Sam, Andy, Mike, Tom, Jeremy, and others who made last summer's internship experience my favorite ever and taught me loads more about faffing around with 3D-printers.

The amazing lads of the Princeton Running Club cannot go unthanked, who have given me a family here at Princeton and a reason to look forward to 4:45 every day.

Finally, thank you to the ECE and SEAS departments, whose funding paid for all of my parts.

Contents

1	Introduction	6
1.1	Relevant Manufacturing Processes	7
2	Methodology	9
2.1	Device and Control	9
2.1.1	Overview of Device	9
2.1.2	Device Control	16
2.1.3	Firmware	17
2.1.4	Toolpath Generation	19
2.2	Design of Multi-Materials	23
2.2.1	Constituent Materials	23
2.2.2	Multi-Material Geometries	25
2.2.2.1	Cement-Silicone Component	25
2.2.2.2	Cement-Polymer Component	27
2.3	Testing	29
3	Results	32
3.1	Data Preprocessing	32
3.2	Fracture Toughness Test	34
3.3	Three-Point-Bending Test	39
4	Conclusion	43
Appendix A	Engineering and Industrial Standards	47
References		48

1 Introduction

There has been a rising interest in the additive manufacturing of construction materials such as concrete in recent years [1] due to its potential for overcoming the geometric constraints of traditional manufacturing techniques while enhancing the mechanical responses of engineering materials compared to conventionally cast components [2] as well as reducing construction costs [3]. There is potential for concrete additive manufacturing to become a promising construction technology in the near future due to these benefits, with the ability to revolutionize the industry and become a pathway for addressing the global housing shortage by allowing for more resilient and sustainable construction [4, 5, 6]. However, despite recent advancements in the field, current concrete additive manufacturing technologies at both small and large scales fail to fully take advantage of the three-dimensional nature of the 3D-printing process and control the material arrangements (architecture) of components using more than one material. This would allow for the reinforcement of additively manufactured concrete components, enhancing the inherently weak tensile strength and brittle nature of the material. Almost all current implementations print with only one material (concrete) due to technological challenges of dual-extrusion processes [7]. Instead, concrete manufacturing is performed using a single-material layer-by-layer extrusion process [8] which can be carried out at a desktop scale or using larger-scale gantries or robotic processes [9]. When reinforcement has been incorporated into concrete additive manufacturing, the solutions have been rudimentary and are not sufficiently automated for integration into the additive manufacturing process, requiring manual intervention [10, 11, 12, 13]. These technological gaps have not only prevented further adoption of concrete additive manufacturing into the conventional construction sector, but they also hinder researchers and practitioners in using the technology to develop new structural engineering materials. Here, a new multi-material additive manufacturing processing technique and platform is presented that addresses a major technological gap that has hindered research in concrete additive manufacturing in recent years. Using this technique, two or more materials are deposited in a layer-wise manner in various arrangements which allows for the creation of (i) new architected multi-materials, (ii) new reinforcement strategies, and (iii) new material-specific

processing techniques.

This work consisted of an initial exploration into automated multi-material cementitious 3D-printing, resulting in a machine that carries a new multi-material cement paste additive process capable of producing new types of cement multi-materials. While the techniques here apply to the field of concrete 3D-printing as a whole, the device developed 3D-prints cement paste, or concrete without coarse aggregates, due to its desktop-scale gantry and smaller nozzle size. This research consisted of two parts: the ***device and its associated control*** and the ***fabrication of the cement multi-materials*** themselves. The device uses a tool-changing 3D-printing platform that combines the constituent materials autonomously, in situ to the printing process to form geometrically complex cement multi-material components. Once loaded with the necessary materials, it requires no manual interaction by the user by following toolpaths generated with a custom software workflow that incorporates control parameters tailored to the complexities of multi-material extrusion. The cement paste multi-materials investigation consisted of using the system to perform a cursory investigation into the architected materials that could be achieved by combining cement paste with other materials in geometrically complex ways. This involved developing new cement paste reinforcement strategies using cement-polymer and cement-silicone combinations. The cement-polymer multi-material was used to explore a novel cement reinforcement strategy using plastic rebars, while the cement and silicone multi-material was chosen as a natural pairing due to their ambient print temperatures and thermal compatibility. It was used to print a unique layered architecture that improved the material properties of cement by increasing its fracture toughness and post-peak characteristics.

1.1 Relevant Manufacturing Processes

While concrete can be additively manufactured in several ways, the method chosen for use with the tool-changing platform was extrusion-based direct-ink-writing [14]. This allows the concrete, in the form of a cement paste (cement paste was used in this work due to the smaller nozzle size being used and the tendency for larger aggregates to cause blockages), to be loaded into a syringe and extruded via positive displacement pumping into the desired shape [15]. This is a much more compact method of 3D-printing cement compared to others

such as powder-bed 3D-printing [16], and allows for the cement paste tool to be mounted on the device alongside others (Fig. 1), facilitating tool-changing. The silicone was also chosen to be 3D-printed using this type of extrusion. Again, while many other methods exist for printing elastomers (such as stereolithography [17]), no others are capable of extruding material compactly, without the use of a bed or vat of uncured material. Additionally, as will be detailed later, extrusion allowed for the use of off-the-shelf tubes of hardware store silicone, facilitating the easy procurement and switching of silicone materials. Finally, crucial to the success of a 3D-printed extruded paste is its *extrudability*, *buildability*, and its *open time* [18]. A material's extrudability refers to its ability to be pumped through a nozzle and deposited on the build surface evenly without clogs. This parameter must be tuned by adjusting its viscosity while preventing solid-liquid segregation and ensuring it remains buildable. Buildability is a material's ability to hold its shape and not "slump" as additional layers of material are printed on top of it. To do this, its yield stress in its uncured form must be larger than the stress of gravity of the material above it. Finally, the open time is how long the material can maintain these properties before it hardens, in the case of the cement paste or cures, in the case of the silicone. The off-the-shelf silicone was chosen that already possessed these properties, while a cement paste formulation was created to fulfil these requirements.

The polymer deposition method was also chosen to be extrusion-based; specifically, fused filament fabrication (FFF) was used. This process involves forcing a solid stock of thermoplastic filament through a nozzle while heating it past its glass transition temperature [19], allowing it to be deposited in a semi-liquid state into the desired shape and then rapidly cooled. FFF was chosen for the polymer 3D-printing due to its compact size and high compatibility with the tool-changing system. Additionally, FFF is a relatively mature technology, which made it a simple matter to incorporate into the multi-material system and tune its parameters. This was in stark contrast to the concrete and silicone extrusion, both of which required significant tuning of their extrusion parameters, with the cement paste requiring tuning of the material formulation itself.

The device and its control and the multi-materials are discussed in depth in the following sections.

2 Methodology

The device developed consists of a multi-tool 3D-printer that can switch between different printing tools, materials, and print processes in situ to a single job. Using tool-changing, it can fabricate cement-polymer and cement-silicone multi-materials that have complex internal geometries. During this investigation, ***beam components*** were printed using the multi-materials in order to characterize their augmented flexural strengths and fracture toughness. This was done according to ASTM standards C78 [20] and E1820 [21]. The following sections detail the construction of the device itself and the fabrication of the multi-materials.

2.1 Device and Control

The first part of this research involved the 3D-printer itself and the associated software, firmware, and tuning required control the machine and fabricate the multi-material components.

2.1.1 Overview of Device

The machine itself was built upon a commercial tool-changing 3D printer platform and is detailed below with the primary components labeled in Figure 1.

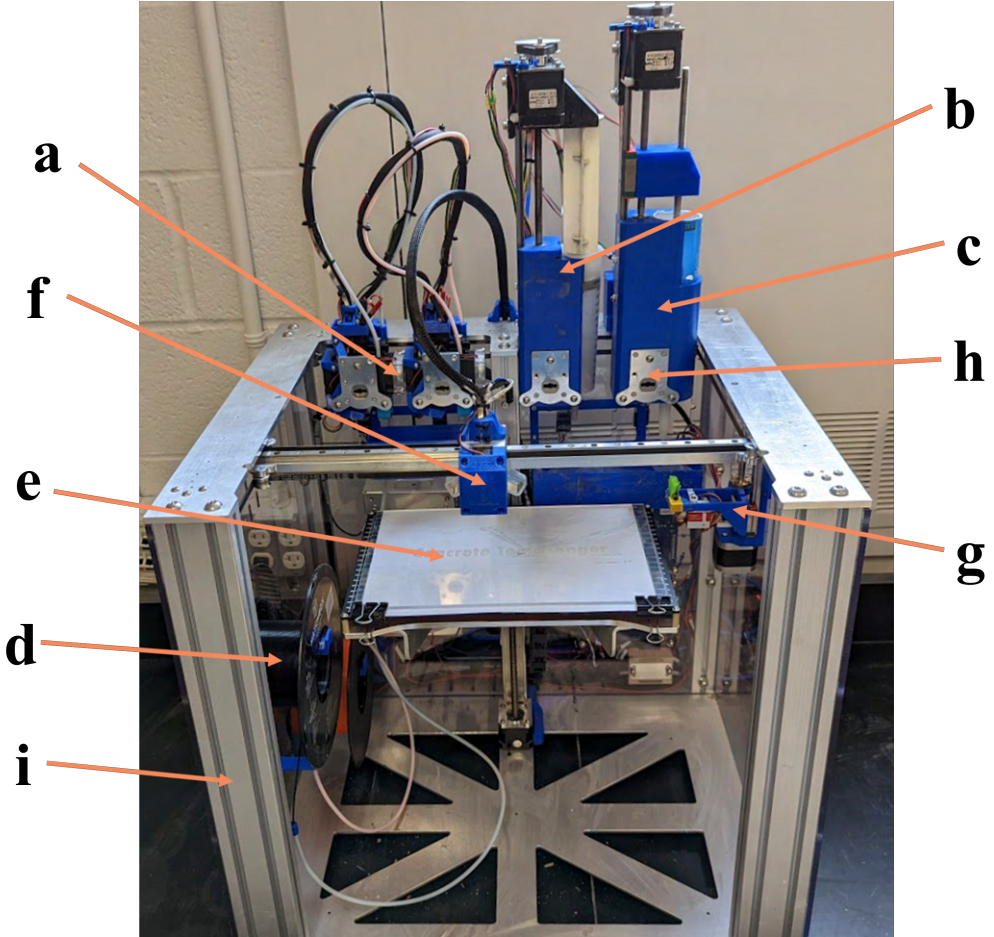


Figure 1: The tool-changing 3D printer that was developed: a. polymer filament-based print heads; b. cement paste extrusion tool; c. silicone extrusion tool; d. material storage/purging; e. build area; f. moveable tool mount; g. polymer print head print preparation; h. kinematically-coupled tool plate; i. machine body.

The tool-changing 3D-printing platform is an E3D ToolChanger [22], and was obtained as an open-source kit consisting of the frame, motion system, and control electronics. The ToolChanger is an excellent platform for this project, as it is extremely open and allows for almost infinite customizability. In essence, it consists of a moveable tool mount (Fig. 1f) that uses a kinematic coupling mechanism to pick up and park up to four different tool heads. Although the kit shipped with four Hemera [23] polymer extrusion tools, these tools could be exchanged for anything that can interface with the tool mount via a tool plate (Fig. 1h) and be parked onto the frame when not in use, as shown in Figure 2. For example, four different polymer extruders of varying nozzle sizes could be used to print different parts of a model at different scales, or additive and subtractive processes could be combined with

the use of a CNC or laser cutter tool. In this case, the current configuration consists of two polymer extrusion tools (Fig. 1a) and two reservoir-based extrusion tools (Fig. 1b and 1c), one for cement paste and one for silicone 3D-printing.

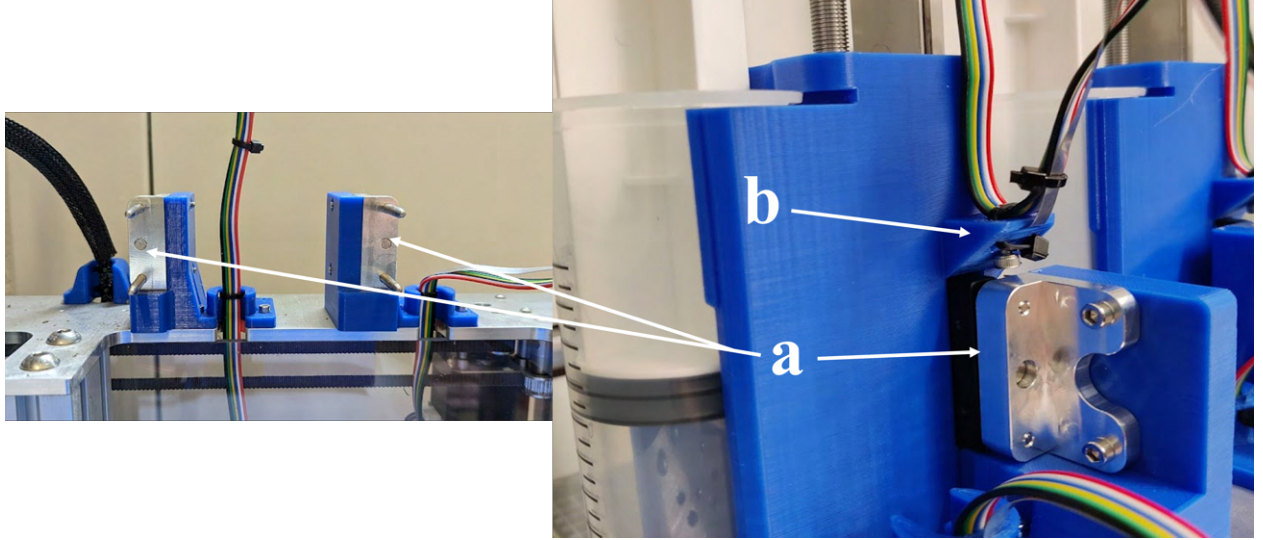


Figure 2: The parking mount for one of the reservoir-based print heads.
a. parking mount; b. new stepper motor wire entry point .

Although the tool-changing kit came with support for polymer extrusion, many other modifications have been made. First are the reservoir-based extruders. They are fairly simple, consisting of a geared stepper motor that rotates a threaded rod, attached to which is a linear rail-mounted depressor which provides the positive displacement necessary to extrude the cement paste and silicone. The starting point for these two extruders were two Hyrel SDS-150s [24], which was purchased and modified with new 3D-printed components to receive a tool plate (Fig. 1b and Fig. 1h) and to interface with the parking mount (Fig. 2a). The entry point for the motor wires was also moved from the top, where the stepper motors are mounted to be just above the parking mount (Fig. 2b). This was to ensure that the wires did not tug on the extruders at the extremes of their ranges of motion, potentially causing jams and introducing print artifacts. It is also important to note that higher torque motors were used for the two extruders, to ensure that they would be able to extrude material for the entirety of the cement paste's open time, even as it began to harden towards the end.

The cement paste extruder is shown in greater detail in Figure 3. It is a less heavily modified version of the Hyrel SDS-150 than the silicone extruder, using the default 150 cc

syringes, the plunger of which is moved by the geared stepper motor (Fig. 3a). In order to print larger objects at a flow rate that could fully utilize the full volume of the syringe within the open time of the cement paste, the stock 3.75 mm diameter nozzle of the of the syringe was left unmodified (Fig. 3b). This also allowed for printing with lower-quality cement powder without clogging, as will be discussed later. Additionally, to facilitate the loading of the cement paste into the syringe, four notches were cut into the rubber seal on the end of the plunger (Fig. 3c and Fig. 3d). This allowed the rubber seal of the plunger to sit directly against the top level of the cement paste once loaded, with no air gap in between, as any air would be able to escape though the notches as the plunger was initially depressed, while the more viscous cement paste was unable to escape through. Eliminating this air gap was essential, as with it proper pressure control of the cement paste was impossible, leading to inconsistent extrusion and frequent jamming.

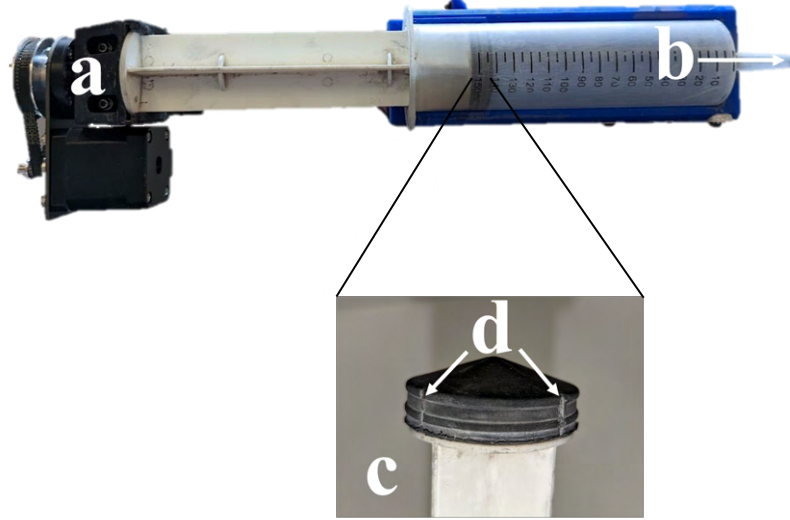


Figure 3: The cement paste extruder: a. geared stepper; b. syringe nozzle; c. plunger head; d. notches cut into rubber seal.

Figure 4 shows the silicone extruder. It is a more modified version of the SDS-150, with the entire body of the extruder having been enlarged to hold the larger silicone tube. The holder for the tube (Fig. 3b) also surrounds most of the circumference of the tube in order to prevent it from buckling as the plunger is depressed, creating high pressures within. This was only required on the silicone extruder, as the walls of the tubes were made of a

much thinner and more flexible plastic than the cement paste syringes. Because the silicone tubes were off-the-shelf hardware store components, their nozzles were able to vary in size depending on how far from the end they were cut. Thus, they were cut at the point where their inner diameter was 3.75 mm (Fig. 4c) to match the nozzle size of the cement paste extruder, facilitating easy layer height compatibility between the two. Finally, the plunger mechanism of the original SDS-150 extruder was modified to accept a threaded rod (Fig 4d) which was threaded into to another 3D-printed component that was hot-glued to the silicone tube's plunger (Fig. 4e). This allowed the geared stepper motor (Fig. 4a) to not only extrude silicone by pressing downward, but retract the plunger for travel moves as well by pulling up on the hot-glued plunger adapter (note retraction was possible on the cement paste extruder as well, however was not performed due to the flow issues it called). Hot glue was chosen because it is a semi-permanent adhesive, still allowing the plunger adapter to be removed from the silicone tube and re-glued to another once the original ran out of silicone.

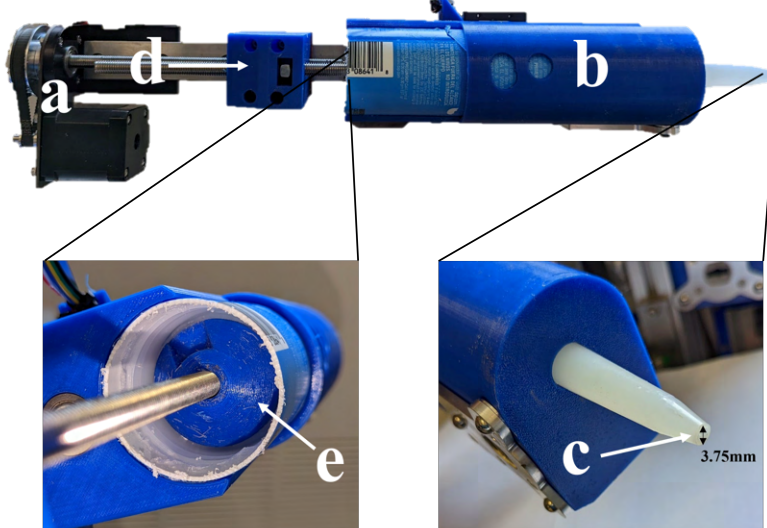


Figure 4: The silicone extruder: a. geared stepper; b. anti-buckle silicone tube holder; c. cut tube nozzle; d. threaded rod adapter; e. plunger adapter.

Before loading the silicone tubes into their extruder, they first had to be cut down, as detailed in Figure 5. This was due to the fact that by default, a significant amount of the tube protruded past the top of the plunger, reducing the available length to extrude with, preventing the silicone tube from being fully utilized. Cutting it down slightly allowed

the draw length of the tube to match that of the SDS extruder's linear rail, reducing the frequency with which the tube needed to be switched out and allowing the full volume of silicone to be utilized, reducing waste.



Figure 5: The modifications made to the silicone tubes: a. original tube length; b. cut-down tube length.

The next modification made was the purge buckets shown in Figure 6. These are designed to catch any ooze that may flow out of both the polymer and reservoir-based print heads. This is so that any oozing material (i.e., ooze drippings) did not interfere with the printer in any way or make their way into the print, causing print artifacts or jamming the print head. The reservoir-based extruder bucket (Fig. 6b) was purged into by the cement paste and silicone extruders just before they began printing after being parked in order to ensure an even flow rate and remove any air bubbles that may have formed while idle. A plastic lining was used (Fig. 6e) for easy cleaning of purged cement paste and silicone between prints. This bucket was also wider than the polymer one, as the purgings from the cement paste and polymer extruders typically amounted to a much higher volume of material during a print. The polymer extrusion bucket had an additional metal wire component (Fig. 6c), which removed any ooze drippings from the nozzle before priming (Fig. 6d), which is discussed next. This removal of larger ooze drippings was crucial, as these larger oozes could not always be handled by the priming process, and ran the risk of being carried into the print. The buckets were also removable, allowing for them to be cleaned.

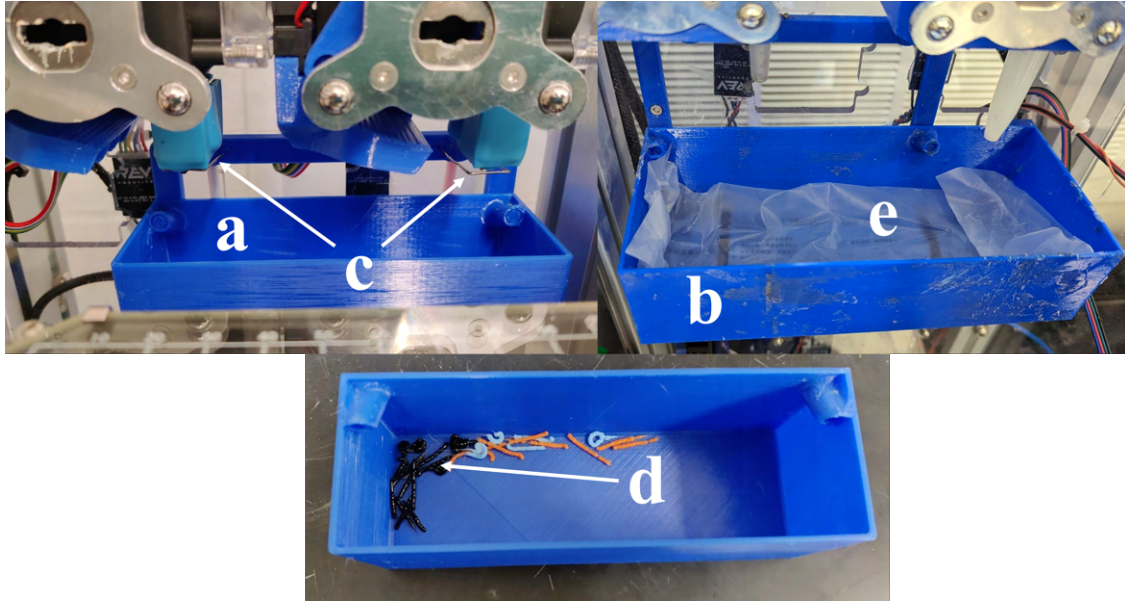


Figure 6: The purge bucket setup: a. polymer extruder bucket; b. reservoir-based extruder bucket; c. ooze dripping cleaner; d. ooze drippings; e. plastic lining.

The final modification made was the polymer print head preparation device (Fig. 1g), as detailed in Figure 7. While the polymer print head was parked, polymer oozed from its nozzle, emptying the melt pool and reducing the amount of melted material readily available for extrusion. Thus, if the print head were to go immediately from idling to printing, the initial extrusion line would be incomplete and uneven. Thus, a prime was needed, wherein the extruder pushed a certain length of filament into the nozzle before printing, filling the melt pool with molten material so that the first extrusion was full and consistent. To do this, a simple procedure was followed. The polymer extrusion tool was picked up by the movable tool mount and vigorously brushed through the silicone brush (Fig. 7a) to clean off any debris that has accumulated on the nozzle. Then, it was moved over the corner covered in Kapton tape, where it extruded a “pebble” of filament (Fig. 5e). This filament was hot, so it adhered to the Kapton tape as the entire component moved down on the linear rail (Fig. 7f). This extrusion was what primed the nozzle, filling it with molten polymer. The device then paused for several seconds while spinning up the part cooling fan to the maximum, allowing the filament pebble to cool, and then vigorously moved through the brush again (Fig. 7g), severing the nozzle’s connection to the pebble. Finally, the servo arm (Fig. 7b) moved to clear the filament pebble away and the part cooling fan was turned off again. Moving quickly

from here to the start of the current layer then ensured that extrusion began immediately without unevenness.

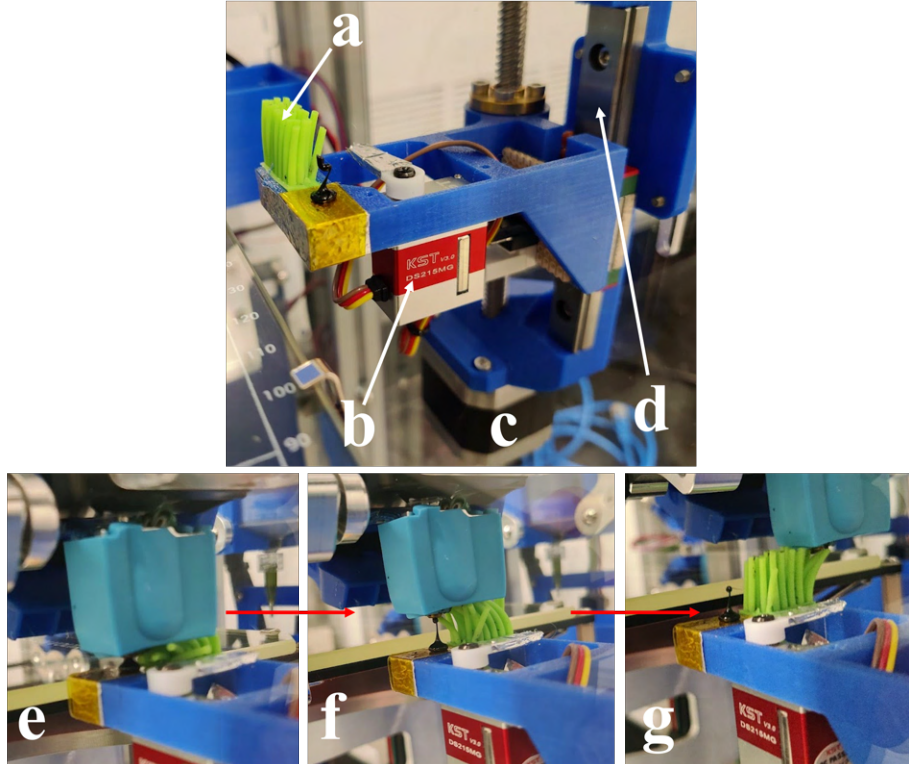


Figure 7: The polymer print head preparation system: a. silicone brush; b. servo motor; c. height adjustment motor; d. linear rail; e. pebble deposition f. cooling move; g. final brush.

The prime process for the reservoir-based extruders was much simpler. After purging, they simply extruded a small amount of material onto an empty portion of the build platform (Fig. 1e) before immediately moving to the start of the current layer’s print path.

2.1.2 Device Control

The device previously discussed cannot function on its own. It requires firmware to control the hardware mechanisms and take in sensor inputs, software to generate the toolpaths that, when followed, generate complex multi-material geometries, and tuning and calibration throughout to tailor control inputs to the machine specifically. Together, these components constitute the ***device control***, and are subject to ***control parameters*** depending on

the tool in use and the material/multi-material being printed. Control parameters include variables such as:

- The thermal compatibility of different materials.
- How to start and stop of print heads of different materials and handle their oozing, purging, and priming.
- The geometries of each tool head, and the limitations these places on how it can print.
- Tool-changing handling to take into account each of the above.

These parameters must be accounted for by every component in the system and at every stage of its development for it to be successful. The following sections detail how they are being accounted for by the firmware and software of the system.

2.1.3 Firmware

The control electronics for the 3D-printer consist of a Duet 2 board, which uses a 32-bit microprocessor running RepRap Firmware (RRF) 3.0 [25]. RRF is an extremely powerful control paradigm for multi-tool 3D-printers, and it is truly what makes the E3D ToolChanger platform so versatile. It supports a wide range of features not found in other 3D-printer firmwares, particularly with respect to RRF's advanced G-code and M-code commands. Typically, G-code commands are simply used to move a CNC device's tool to a specific xyz-location at a particular feedrate, with M-codes being used to control auxiliary parameters, such as tool temperatures, fan speeds, accelerations, and the like [26]. In RRF, however, the G-code and M-code commands are much more akin to a programming language. They can interface with deeper settings of the printer with the ability to change parameters that would typically have to be configured in a printer's firmware. RRF's G and M-code commands can configure tool definitions, assign endstop pins, and even read sensor inputs. Additionally, it is possible to run custom G-code macros (sequences of G-code commands that can be saved as files on the microprocessor and called by *other* G-code commands *in situ* to printing), and use basic scripting features such as *if* statements, *for* loops, and variable declarations within the G-code itself. Each Duet board can also support a large number of inputs and

outputs, with vast expansion possible through expansion boards. For this device, a DUEX 5 expansion board was used, which has the capacity to support up to seven tools. Finally, this is all controlled through a built-in web interface running on the microprocessor itself, making it very easy for the user to interact with the device over a network.

In the context of the device that was developed, several of these features were taken advantage of. Custom G-code macros were used to define the move sequences for homing the printer, switching between tools, and purging/priming the tools before use. RRF automatically calls the scripts `tpreTOOLNUM.g`, `tpostTOOLNUM.g`, and `tfreeTOOLNUM.g` before selection, after selection, and before parking `TOOLNUM`, which is any of the four tools from T0 to T3. These allow the specific move sequences and xyz-locations required to pick up, park, and prime tools to be defined locally on the machine itself, rather than in the G-code toolpath of a print. Thus, all the specific tuning parameters related to the tool locations, accelerations, material-specific prime procedures (the cement paste and silicone extruders must be purged by different amounts before printing, for example), and tool offsets were handled on-device. This simplified the toolpaths that need to be generated for the device, as they only needed to issue higher-level macro commands with the lower-level details being handled by the on-device processing. For example, the entire priming sequence for the polymer head described in section 2.1.1 was defined in the macro `prime.g` and was called with a single M-code command from the toolpaths.

The scripting features available within RRF have also proven useful. Each print, several global variables were set by the toolpath G-code during its startup sequence which were used by the printer during the print. The first was the variable `global.printing`. It was set to `true` during a print, and the `tpostTOOLNUM.g` and `tfreeTOOLNUM.g` macros checked this variable when called during tool changing, purging and priming. `global.printing` was then set to false at the end of the toolpath G-code. This was done so that when selecting tools during normal use, such as for loading materials and preparing for a print, the purge and prime sequences were not executed every time, wasting material.

The cement paste priming sequence also relied on this feature. In order to ensure that the cement paste was flowing evenly before starting a layer, it first extruded a prime line of between 50-100 mm. To save on print area, the prime line for a given layer was deposited on

those before it, forming a vertical stack. However, depending on the geometry being printed, cement paste was not used every layer, so the prime line could not be printed at the current z-height. Thus, the variables `global.cementPrimeLayer` and `global.cementPrimeZ` were used within in the macro `cementprime.g` to keep track of the prime layer number and the layer height of each extrusion. `global.cementPrimeLayer` was set to 1 at the start of a print by the toolpath G-code and then incremented after each prime move. Several other parameters were set at the beginning of the toolpath G-code, such as `global.cementPrimeX`, `global.cementPrimeY`, and `gloal.cementPrimeLength` which dictated other parameters of the prime. With this, each time the geometry needed to switch to the cement paste tool, the `cementprime.g` was called and the cement paste priming was handled automatically on-device, independent of the toolpath G-code.

An example of how these variables were used is shown below in Figure 8 in the two code snippets.

```

11 ; start G-code
12
13 ;start printing
14 set global.printing = true
15
16 ; set concrete purging variables
17 set global.concretePrimeLayer = 1
18 set global.concretePrimeX = 215
19 set global.concretePrimeY = 125
20 set global.concretePrimeZ = 2.7
21 set global.concretePrimeLength = 60
22 set global.concretePrimeE = 0.9

1 ;concreteprime.g
2
3 var primeZ = global.concretePrimeLayer * global.concretePrimeZ
4
5 G1 X{global.concretePrimeX} Y{global.concretePrimeY} Z{var.primeZ} F7000
6 G1 X{global.concretePrimeX+global.concretePrimeLength} E{global.concretePrimeE} F600
7
8 set global.concretePrimeLayer = global.concretePrimeLayer + 1

```

Figure 8: Two code snippets demonstrating how G-code macros, scripting, and toolpath generation were combined using RRF. Left: a snippet of the start G-code from a toolpath; Right: the cement paste priming macro that uses the variables set by the start G-code.

2.1.4 Toolpath Generation

Each print performed by the printer was carried out by following a sequence of G-code commands that form a toolpath. Following G-code commands was relatively simple from the printer's point of view; however, generating this toolpath can be very challenging, especially for complex multi-material geometries, and thus was a large focus of this work. Traditionally, 3D-printer toolpath generation is done as described in Figure 9. A design is modeled in a computer aided design (CAD) program and exported as a mesh to a slicing program, which

splits the 3D object into 2D slices and generates the G-code commands required to deposit the material in the shape of each layer, taking into account settings such as extrusion amount, infill percentage, number of perimeters, and so on.

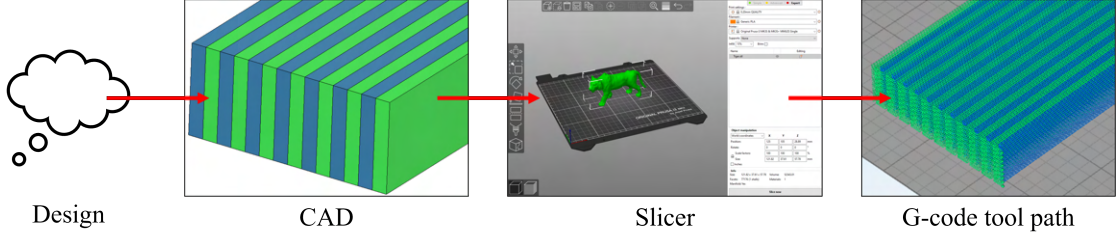


Figure 9: The pipeline traditionally used to generate a toolpath from a design.

While this process works extremely well for the vast majority of 3D objects, it is less well suited to multi-material 3D-printing, especially in cases where it is necessary to directly control the extrusion parameters and interaction between different materials. For instance, in the CAD model shown above, it may be intended that each of the interlaced sections consist of single or side-by-side extrusions. However, depending on the perimeter and infill settings of the slicer, as well as the size of the interlaced sections, it may design a toolpath that uses perimeters and sparse infill, rather than printing each interlace completely solid. While it is possible to tune slicing settings to achieve a specific toolpath, doing so is often a tedious and indirect process, as it is often unclear how various slicing parameters will interact with each other and affect the final output. Thus, for this work, the pipeline shown in Figure 10 was used.

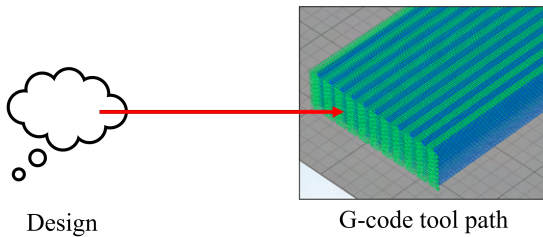


Figure 10: The pipeline used to generate toolpaths for this work, ideal for direct control over processing parameters.

Using this pipeline, the CAD modeling and slicing steps were skipped altogether, and the toolpaths were generated directly from a part design. This was done using a tool called

FullControl [27]. It is a Microsoft Excel-based tool that allows the user to define custom toolpaths without having to use CAD or a slicer. It does this by using Excel's built-in function, scripting, and variable functionalities to convert high-level commands such as a line or rectangular feature into G-code commands. A screenshot of the interface is shown in Figure 11.

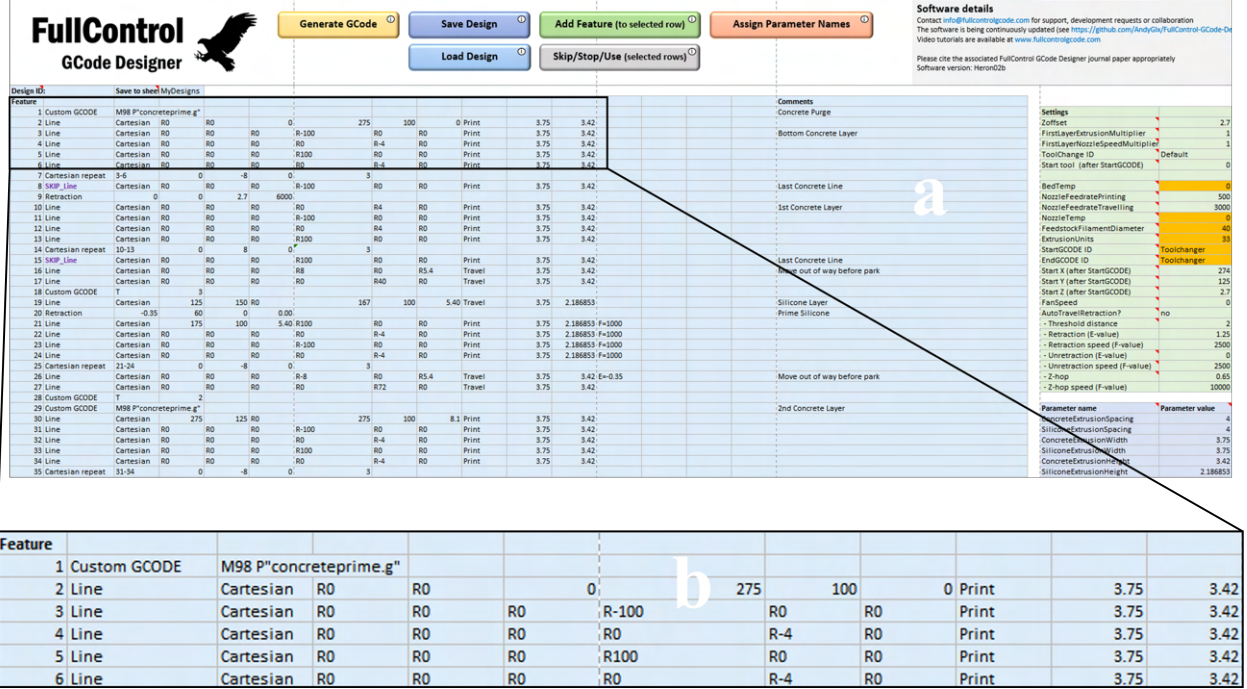


Figure 11: The FullControl Excel interface: a. overall interface; b. a zoomed-on view of a few of the print features from a design.

Each toolpath design consists of any number of print features. They can be cartesian lines, repeat features (in which several features can be repeated multiple times), and even polar coordinate lines. Each feature is converted into a sequence of G-code commands as needed, with every parameter controllable, such as the start and end coordinates of a line, the movement speed, and the extrusion width and height. Using Excel's function and variable capabilities, these lower-level parameters can all be determined parametrically in response to high-level design requirements such as the height, width, and span of a beam. Combining these simple features together can create very complex geometries that would be impossible to recreate in a traditional slicer such as non-planar printing gradient-wise variations of parameters throughout a print. This level of control was essential for this work, especially

in designing the multi-material geometries. Additionally, low-level control such as this made it simple to interface with the custom macros of the Duet and RRF firmware, as commands to call certain macros or check certain sensor inputs can be inserted at any point as a print features.

For a given line of extrusion, tuning the extrusion width, height, and spacing was essential to ensuring even extrusions and the proper interfacial properties between extrusions of the same and different materials. For a given print line, the quality of extrusion was determined by the E-value of the G1 command shown in the example below:

$$G1X200Y175E2.465F1200 \quad (1)$$

This dictates to the printer how many millimeters of material stock to extrude; millimeters of filament for the polymer extruder and millimeters of plunger depression for the cement paste and silicone extruders. This value is calculated according to the following equation:

$$E = \frac{4H_E}{\pi d_{stock}^2} (W_E - H_E(1 - \frac{\pi}{4})) \cdot L_E \quad (2)$$

where E is the G-code E-value, H_E is the extrusion height, W_E is the extrusion width, L_E is the extrusion length, and d_{stock} is the diameter of the material stock. This was derived assuming the nozzles and stock materials are circular resulting in extrusions in the shape shape below in Figure 12.

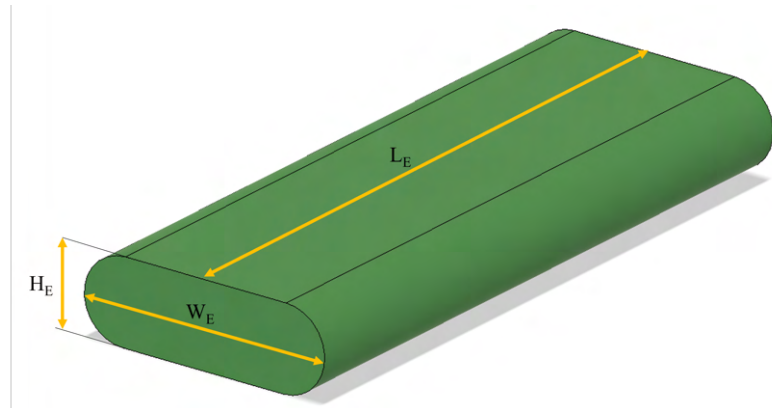


Figure 12: The assumed shape of the material extruded from the polymer, cement paste, and silicone extruders

In FullControl, each of these parameters were fully customizable and tuned such that extrusions were smooth and interfaced with their neighbors without being over-extruded at the chosen layer height. 2.7 mm was chosen as the layer height for all the prints described in later sections. This layer height is just under 75% of the nozzle widths of the cement paste and silicone extruders, which is generally the largest layer height to nozzle diameter ratio possible before uneven extrusion starts to occur and the extrusion shape no longer matches that of Figure 12. Additionally, the Hemera polymer extruder had a nozzle diameter of 1.2 mm, meaning its maximum allowable layer height was 0.9 mm, which is exactly one third of the cement paste and silicone layer height, allowing for integer ratios of layers during multi-material prints. The extrusion width, referring to how far the tool head physically moves between adjacent extrusions, was tuned to 4 mm for the cement paste and silicone extruders and 1.35 mm for the polymer extruders to allow for some over-extrusion and proper interfacial bonding. Finally, d_{stock} was set to 1.75 mm, 40 mm, and 48 mm respectively for the polymer, cement paste, and silicone extruder to match the filament, syringe, and silicone tube diameters.

2.2 Design of Multi-Materials

The second part of this work was related to the design and characterization of the multi-material components themselves. Using the device and toolpath generation process described above, a preliminary investigation was made into two types of multi-materials: **cement-polymer** and **cement-silicone**. Their design and fabrication are discussed in the following sections.

2.2.1 Constituent Materials

Used in both multi-materials was cement in the form of cement paste. After extensive tuning according to the principles described by Rodriguez et al in [18], a mix design was developed that was the best combination of extrudability and buildability achievable in the time available. Due to supply constraints, a lower-quality cement powder that was more prone to clogging had to be used. Thus, the final mix design was less buildable than would

normally be optimal, and the stock 3.75 mm syringe nozzle had to be used as opposed to smaller, more detail-capable nozzle sizes to further reduce the likelihood of clogging. These issues were despite initially sifting each cement powder using increasingly-fine sieves to a passing particle size of 150 μm . The components of the mix design included Buzzi Unicem cement powder, Gelanium 7700, and VMA 362 which together worked to modify the rheological properties of the stock cement-water mixture to allow it to be printable. The mix design is summarized below.

Table 1: Cement Paste Mix Design	
Component	Volume %
Cement Powder	58
Water	3
Gelanium	1
VMA	3

The component materials were mixed with a two-stage mixing cycle using a Renfert Twister Evolution vacuum mixer. In between each stage, the cement paste was manually mixed using a scraping tool, to ensure all the solid components would be fully integrated during the second mix stage. The scraper was then used again to transfer the cement paste from the mixing container to the syringe, with care being taken to avoid introducing air bubbles into the mixture (note this was impossible to avoid fully, with small air bubbles occasionally leading to uneven extrusions). Finally, the full syringe was loaded into the printer and the print could begin.

Once printed, the cement paste components were placed in a humidity chamber with a relative humidity above 85% to harden for seven days. On the seventh day, they were removed from the chamber and tested according to the procedures described later.

For the cement-polymer multi-material, polylactic acid (PLA) was chosen as the polymer. This was due to its high tensile strength relative to hardened cement paste (HCP), making for an ideal material for a rebar architecture, while being able to be printed at relatively low printing temperatures, both in terms of the nozzle and bed temperature. This was important, as printing the cement paste too closely to a hot component was found to

partially evaporate the water from the mixture, leading to cracking of the paste before full curing and a reduction in final strength. The PLA was printed with a nozzle temperature of 220 °C, which allowed it to quickly cool down to close to room temperature while switching to the cement paste extruder. The PLA was also able to be printed without a heated bed, further reducing the temperature impact on the cement paste. Instead, the print surface was treated with blue painter’s tape, whose texture made for ideal bed adhesion, allowing for quality prints while avoiding drying out the cement paste.

The cement-silicone multi-material was fabricated using the DAP clear silicone. This was an off-the-shelf hardware store grade room temperature vulcanization (RTV) silicone with a cure time of 24-48 hours. It was chosen due to its favorable print qualities, being easy to extrude from the silicone extruder with virtually zero air bubbles while remaining buildable for the heights of the objects fabricated.

2.2.2 Multi-Material Geometries

Described in this section are the two multi-material geometries that were printed and tested during this investigation. The dimensions were chosen to target the requirements laid out by ASTM C78 and E1820 while being integer multiples of the extrusion spacings and layer heights. Thus, (span x width x depth) dimensions of (100 x 32 x 27) mm were targeted. Once printed, the final dimensions of the parts varied due to slump in the cement paste and inaccuracies in the printer’s gantry movement, however these discrepancies were taken into account by measuring true final dimensions during the strength calculations.

2.2.2.1 Cement-Silicone Component

The cement-silicone multi-material beam consisted of a simple layered architecture, as shown in Figure 13. This was chosen in the hopes that the flexible silicone layers between the brittle HCP ones would improve the beam’s fracture toughness due to the additional flexibility provided by the silicone. Each cement-silicone beam consisted of five cement paste layers with four silicone layers in between each one. The bottom layer was ”doubled up,” with two adjacent cement paste layers stacked on top of each other in order to provide enough thickness for the samples to be notched and tested for fracture toughness.

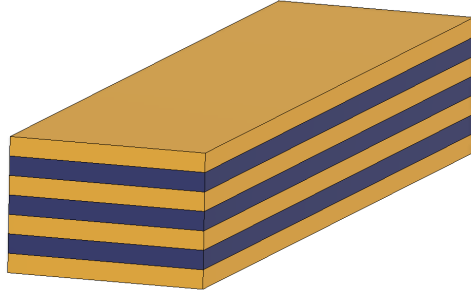


Figure 13: A CAD representation of the cement-silicone component: cement paste layers are in yellow; silicone layers are in blue.

The toolpath design for this component was fairly simple, with each layer consisting of side-by-side cement paste or silicone extrusions, with a tool change in between each. Each extruder performed its prime maneuver as was discussed earlier in section 2.1.4 before starting each layer. Figure 14 depicts the multi-material printing process,

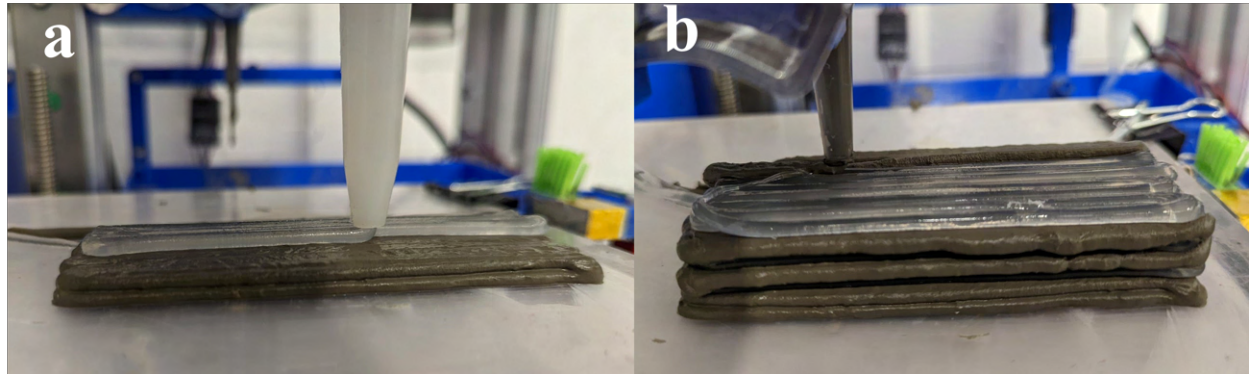


Figure 14: The multi-material printing process of printing a cement-silicone beam:
a. silicone on top of cement paste; b. cement paste on top of silicone.

while Figure 15 shows the final component after seven days of curing. Note that small amounts of interfacial bonding occurred between the HCP and silicone layers, holding the different layers together to form the multi-material component.



Figure 15: The final printed cement-silicone beam: a. front view; b. side view.

2.2.2.2 Cement-Polymer Component

The cement-polymer multi-material component was designed to emulate traditional concrete reinforcement strategies that employ materials of high tensile strength, such as steel, as rebars to improve the tensile strength of a concrete beam. Thus, this architecture consisted of three plastic rebars encased in cement paste extrusions. Because the PLA polymer used had a much higher tensile strength than the HCP, the intention was for the PLA rebars to significantly increase the peak load the beams were capable of supporting. Unlike traditional rebars, the plastic ones had to fully extend to the bottom layer of the print, as the PLA would only adhere to the painter's tape build surface, not uncured cement paste. Thus, barbs were incorporated into the lengths of the rebars to increase the mechanical bonding between the two constituent materials, as no chemical bonding occurred between the cement paste and PLA (similar to how barbs are added to steel rebars in traditional fabrication methods). Figure 16 shows a CAD representation of the beam.

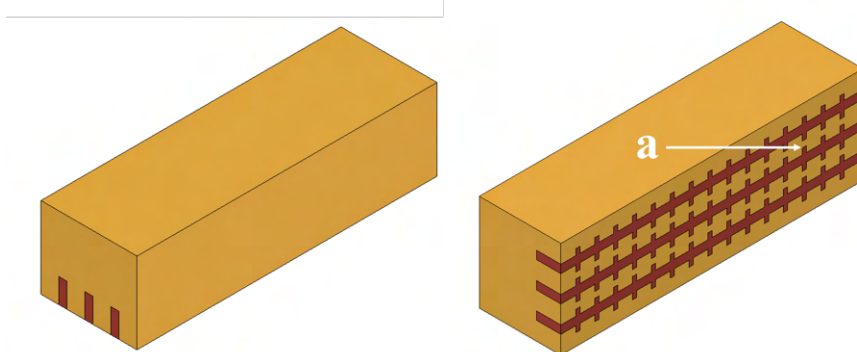


Figure 16: A CAD representation of the cement-polymer component: cement paste layers are in yellow; plastic rebars are in red; a. rebar barb.

The toolpath design for this component was more involved; because the layer height of the polymer extruder was one-third of that of the cement paste and silicone, three layers of PLA had to be printed in a row before switching to the cement paste tool. Then, because the syringe nozzle was much wider than the polymer extruder's, it was unable to fit in between the PLA barbs, so instead the cement paste extuder made a single pass past each rebar, over-extruding significantly (done by increasing the extrusion height/width in FullControl) in the process to allow the cement paste past to flow into the gaps between each barb. Once the polymer rebars had reached their full height, The cement paste extruder then extruded normally on top of what had been printed until the full beam had been printed. This process is shown in Figure 17.

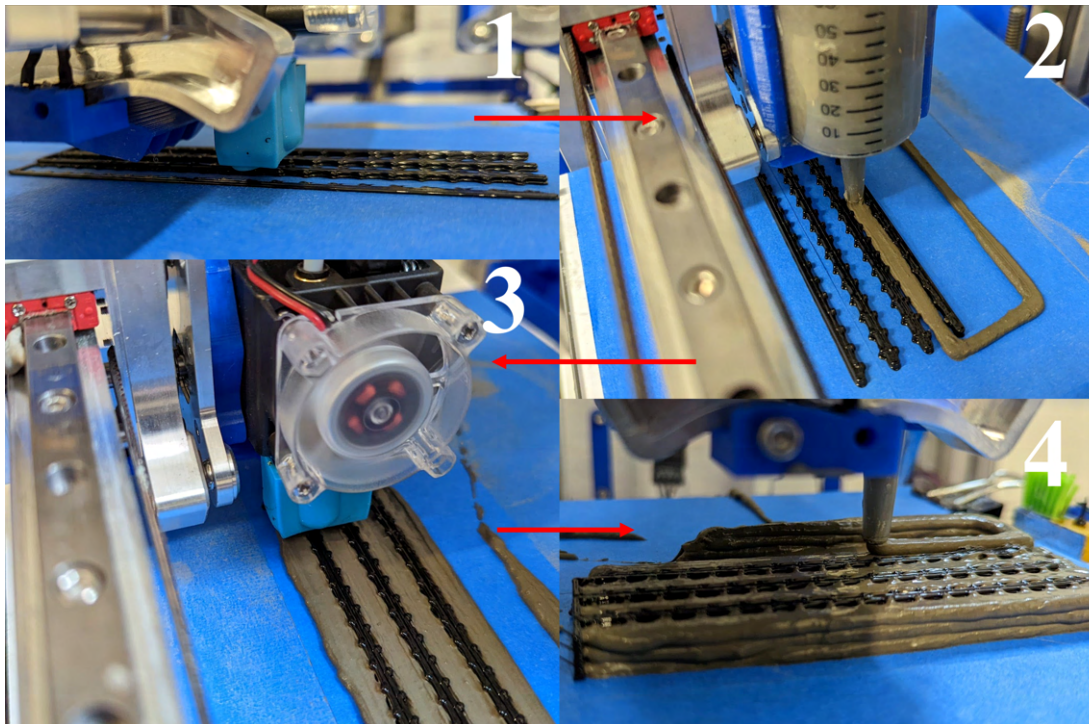


Figure 17: The process for printing the polymer rebar multi-material component:
 1. three initial layers of barbed polymer rebar; 2. rebar barbs are filled in by over-extruded cement paste; 3. the next three layers of polymer are printed and the process repeats; 4. the rebars are fully encased in cement paste as the rest of the beam is printed in a single material.

Figure 18 shows the final component after seven days of curing.

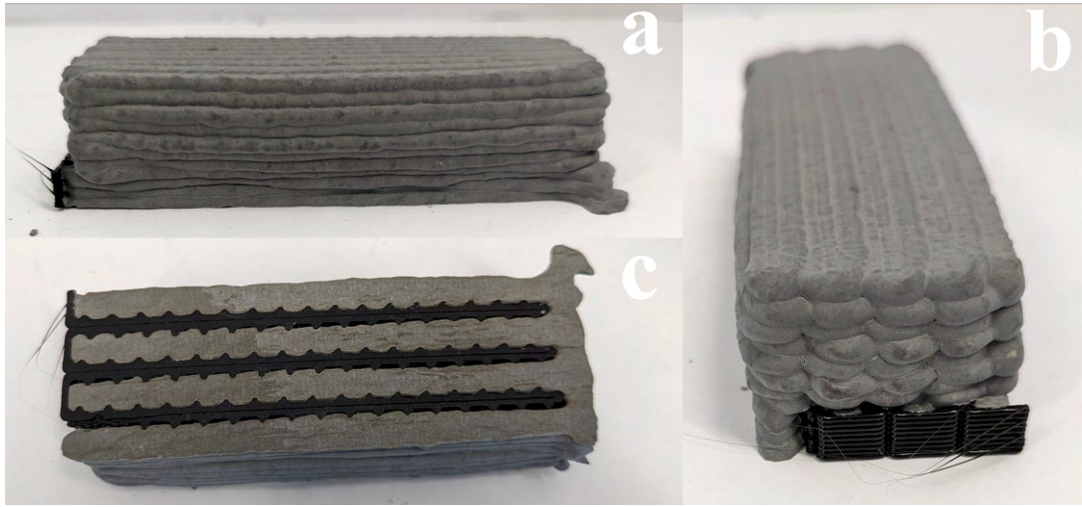


Figure 18: The final printed cement-polymer beam: a. side view; b. front view; c. bottom view.

2.3 Testing

Both geometries were subject to a three-point-bending (3PB) test according to ASTM C78 to evaluate their overall toughness and modulus of rupture (MOR), while the cement-silicone component was subject to an additional fracture toughness test according to ASTM E1820. To perform these tests, a MTS C45.305Y Universal Testing Machine was used to apply a load at a test rate of 0.1 mm/min and a MTS 632.02e-20 extensometer was used to measure crack mouth opening displacement (CMOD) at the notch. Each test was performed on three different samples of each type to assess repeatability and to generate confidence intervals for the calculated values. For comparison, both tests were also performed on cast samples and fully cement paste 3D-printed samples (from here referred to as "solid" samples), as shown in Figure 19.

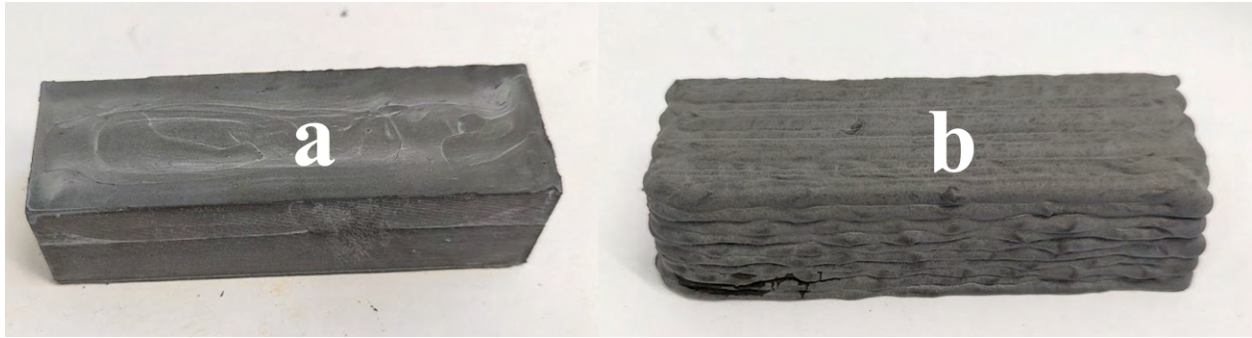


Figure 19: The two samples used to compare the multi-material geometries against: a. cast beam; b. fully cement paste 3D-printed beam.

For the fracture toughness tests, each sample was notched to facilitate crack initiation. This was done in a two-stage process; initially, a wider trough was cut using a hacksaw, which was then narrowed down to a fine point using a razor blade. This notch was only made into the first HCP layer for the printed samples, with the layered cement-silicone ones having been printed with two cement paste layers first before the first silicone one. In order to ensure that the extensometer could accurately measure the CTOD, two razor blades were positively attached to each sample on either side of the notch using hot glue, as it was too large to fit into the small cracks made. A notch depth of 1mm was targeted for each. This process is depicted in Figure 20.

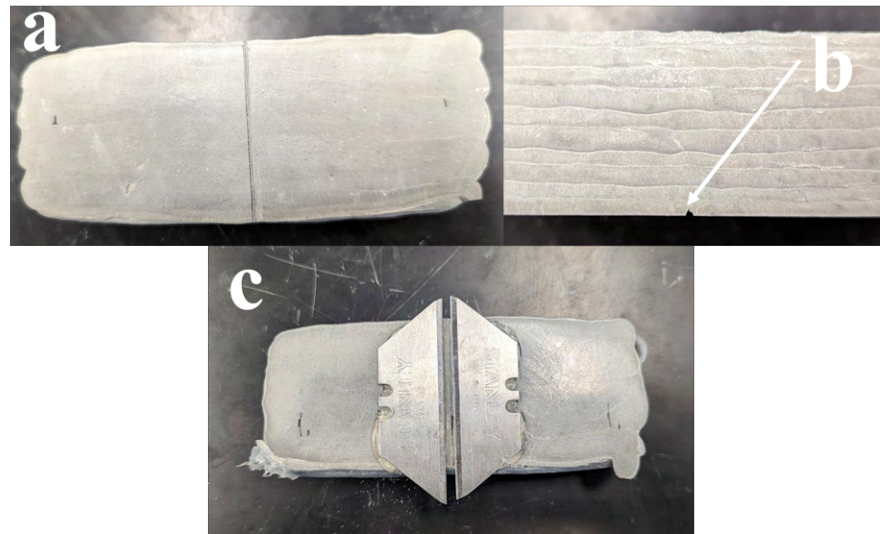


Figure 20: The process of notching a sample for the fracture toughness test: a. notch made using a hacksaw then sharpened with a razor blade; b. fine tip of notch made using razor blade; c. positively-attached razor blades for extensometer.

A camera also took continuous video recordings during each test in order to correlate the load-displacement data with visual images. An example test setup is shown below in Figure 21.

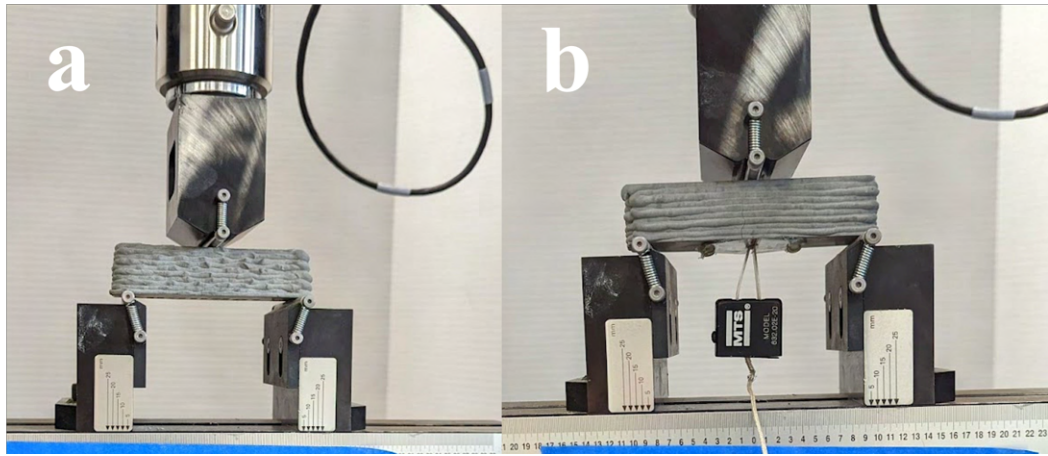


Figure 21: The test setup for the beam components: a. three-point-bending test; b. notched fracture toughness test with extensometer.

Before each test, each sample's width and height was measured in three different places

along its span and averaged according to the sample preparation standard ASTM standard C31 [28], as required by ASTM C78 and E1820. These dimensions, as well as the mass of each sample, were used to normalize the results to the size and density of each sample and in other calculations, such as the stress.

3 Results

The load-displacement and load-CMOD data was exported from the MTS machine in the form of .csv files, which were then analyzed using Python scripts. This process as well as the results of the analysis are described in the following sections.

3.1 Data Preprocessing

Typically, when subjecting brittle materials such as cement paste to a three-point-bending test, it is expected to see a linear, elastic relation in the load-displacement curve up until the peak load, until a brittle failure occurs, fracturing the sample and returning the load to zero (almost) immediately. This results in little to no post-peak softening with a negligible plastic region. While this was the case with the cast samples, the solid, cement-silicone, and cement-polymer samples all experienced post-peak softening to varying extents, with the cement-silicone even experiencing multiple load peaks. Thus, it was necessary to first identify the initial peak, so that the elastic and plastic regions could be separated. Example load-displacement outputs from a cement-silicone and cement-polymer sample are shown in Figure 22, with the initial peaks identified (Fig. 22a). This peak index was then inputted into the Python script so that it could linearize the load-displacement curve up to the initial peak (Fig. 22c), which assisted with later analysis and accounted for movements and other inaccuracies within the MTS machine itself.

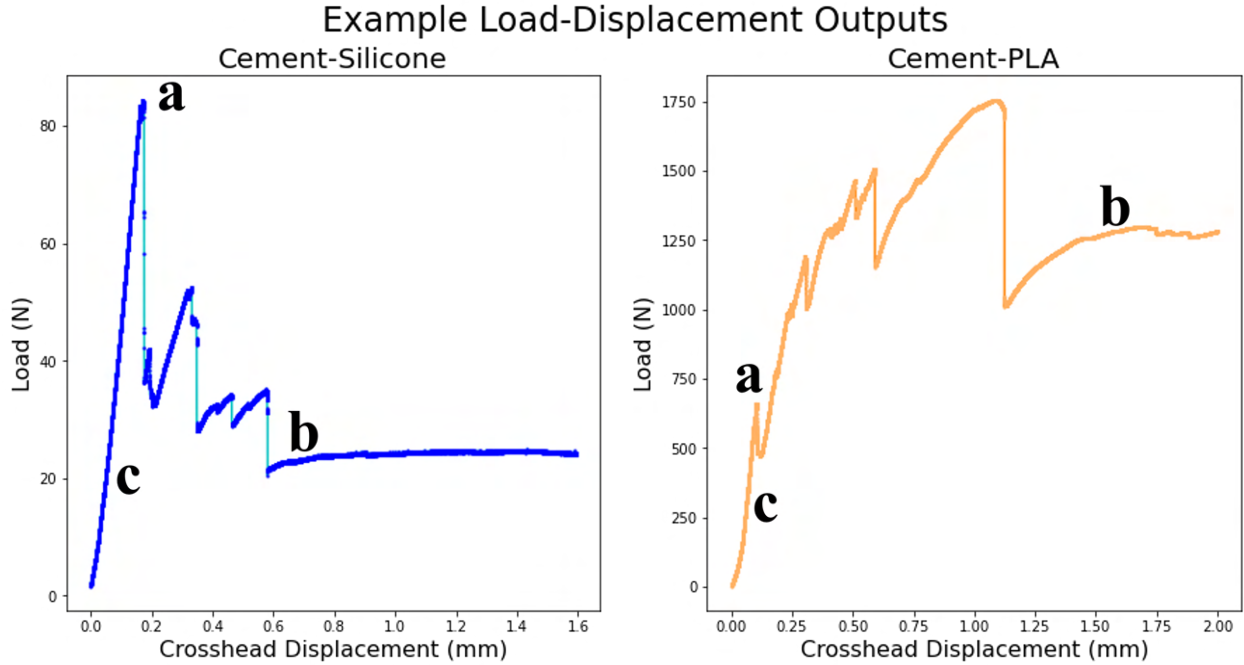


Figure 22: An example load-displacement output from a cement-silicone beam (left) and a cement-polymer beam (right): a. initial peaks; b. plateau regions; c. section of curve to be linearized.

The Python scripts found peaks automatically when reading in a load-displacement file along with a list of the associated indexes, as shown in Figure 23. With these two things, the user could manually define the first peak and run the rest of the analysis with the linearized data.

```
[ 59  4025  4886 11140 12972 13568 14038 20446 22600 30090]
```

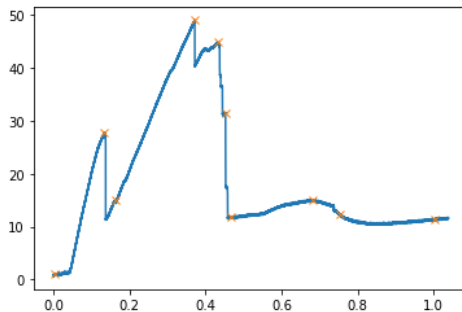


Figure 23: An example load-displacement output from the Python script. Peaks are marked with an orange 'x'

The next preprocessing step was determining the endpoint of the load-displacement and load-CMOD outputs. For the cast and solid samples, this was trivial, as the load

dropped off very quickly after the initial peak, with the end taken to be the point where the load dropped to 20% of the max load, as prescribed by [29]. For the cement-silicone and cement-polymer samples, however, the end point was less obvious, as once all the hardened cement paste had fractured, the beam was still applying significant load as the silicone layers and rebars remained unbroken and continued to flex (Fig. 22b), causing the load to plateau. Given that these tests were designed to test HCP components, the end points were taken to be the points at the beginnings of these plateaus, when the HCP portions of the composites had failed and only the silicone and polymer portions remained. Once manually determined, this end index was also inputted into the Python script, with a cropped, linearized version of each tests' data then used for subsequent analysis.

3.2 Fracture Toughness Test

The fracture toughness tests were primarily aimed at validating the cement-silicone layered concept architecture. It was performed on three different cement-silicone beam samples according to ASTM E1820 as well as three different cast and solid samples for comparison. Analysis to calculate each sample's K_{ic} , K_{jc} , and crack length propagation Δa was done using a mix of formulas from E1820, E399 [30], and the supplementary materials of [31]. Note that the following plots show the results from a single notched cast, solid, and cement-silicone sample that were found to be representative of the entire sample set, however the values given are averages of the entire test set.

Shown below in Figure 24 are the specific load-displacement and load-CMOD plots from the fracture toughness tests. The specific load is defined as the absolute measured loading normalized by each sample's density. From here on, any "specific" measurements defined are the absolute values divided by the specimen's density. This was done due to the fact that the multi-material samples possess less HCP than the cast and solid ones, allowing for comparison across different HCP concentrations. Also note that the lead-up to the each sample's initial peak has been linearized using a least-squares solution for the slope sampling from the last tenth of data points leading up to the initial peak (e.g., if the peak index was 1000, data points 901-1000 were inputted into the least-squares solver). The cast and solid samples have also been cropped post-peak once the load reached 20% of the maximum per

the preprocessing procedure. While the specific peak loads of the cast and solid samples were similar, it was much lower for the cement-silicone sample. This is due to the fact that each HCP layer was only one layer thick (2.7 mm) and thus very fragile. Additionally, the overall HCP content was very low, with only 6/10 layers being made of HCP. However, after the initial peak load, the sample continued to be able to be deformed, with the crosshead and CMOD continuing well past the positions of the cast and single samples. This trend was also observed for the unnotched samples during the 3PB test, indicating the multi-material components were capable of producing much more plastic deformation than their fully-cement counterparts due to the additional flexibility provided by the silicone layers, which experienced only elastic deformation. These results are summarized in figure 25.

Corresponding Cracks in Samples across Load-displacement and Load-CMOD

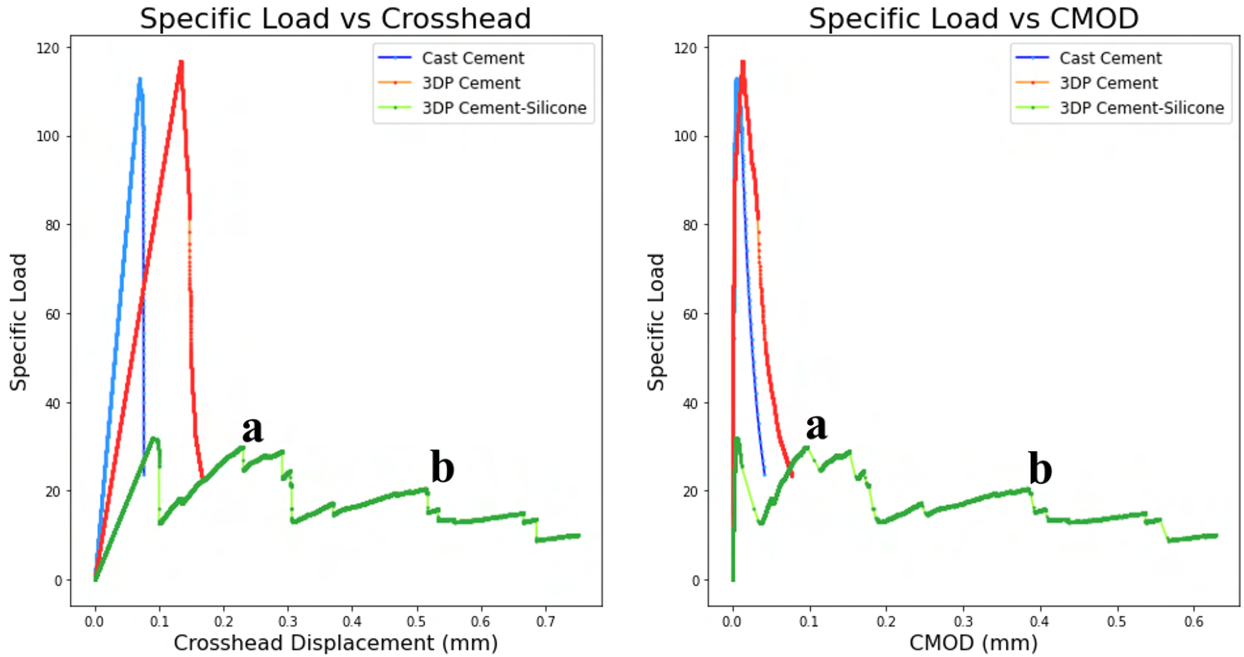


Figure 24: Representative plots of the specific load-displacement and load-CMOD data from the fracture toughness test: a-b. corresponding cracks between the load-displacement and load-CMOD data. Note that these can be found by matching the start and end loads of crosshead/CMOD jumps, as indicated by the light-green lines.

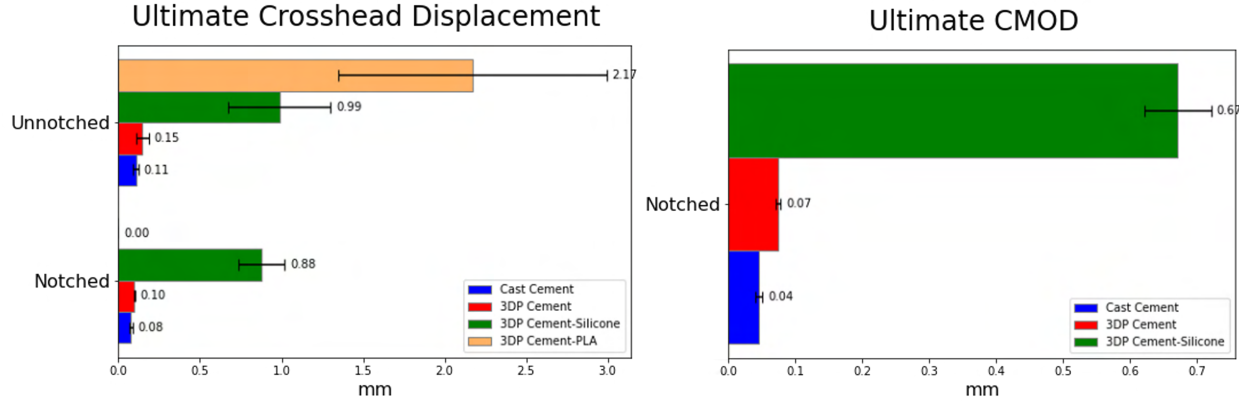


Figure 25: The crosshead (left) and CMOD (right) at the end of each test for the notched and unnotched samples. End point taken to be at 20% of peak load for cast and solid samples and start of plateau for cement-silicone ones.

Another significant result is the multiple cracks experienced by the cement-silicone sample. These are indicated by a steady increase in load followed by a sudden drop, which can be seen in the light-green portions of the load-displacement and load-CMOD curve where the data points are more spread out (Fig 24a-b). These cracks were spread out compared to the single cracks experienced by the fully-cement samples, as each silicone-separated layer of HCP was subject to different amounts of tensile stress depending on where in the stack it was located. As a lower layer of HCP cracked, the tensile stress would be transferred to the silicone and next HCP layer above it. This allowed for it to withstand much more strain and movement from the crosshead, as is shown in Figure 25. Additionally, as shown in Figure 26, the cracks spread disjointedly from one HCP layer to the next. The crack paths were broken up by the interspersed silicone layers, which even resulted in multiple cracks forming on the same layer.

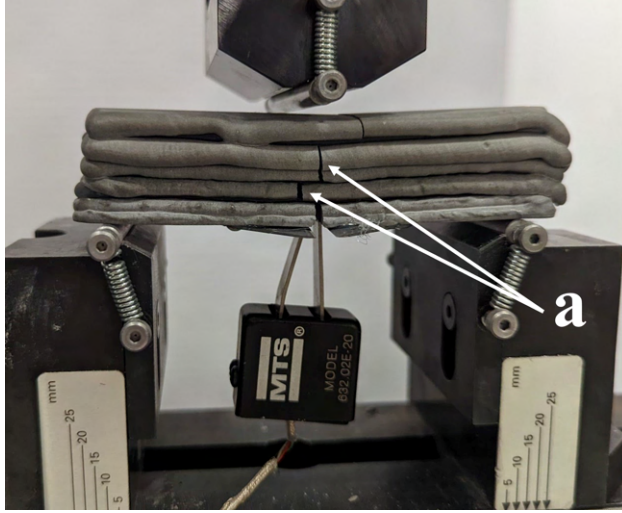


Figure 26: A cement-silicone sample just after the completion of a fracture toughness test with the extensometer still installed: a. the discontinuous crack propagation pattern between silicone layers.

Using the load, displacement, and CMOD data, it was then possible to calculate the K_{ic} and K_{jc} to characterize each sample's elastic and plastic fracture toughnesses . This data was also used to calculate the crack extension Δa to generate an R-curve, as shown in Figure 27. Note that the cast samples failed in a brittle manner and thus have a K_{jc} of zero, while the solid samples did exhibit some softening (as can be seen in the post-peak response in Figure 24), and thus has a non-zero K_{jc} . Note also that ASTM E1820 considers a sample failed once the crack length extension surpasses 20% of the uncracked ligament (the difference between the nominal depth of the sample and initial notch length). This is demarcated with a gray dotted line in Figure 27, and it is at this crack length that the K_{jc} values for the solid samples were taken, thus the Δa and K_{jc} values past that point are less meaningful. However, this is not necessarily the case for the cement-silicone composite. As was shown in Figure 26, there is no single crack path being taken between silicone layers, so the Δa being calculated is more of an *effective* crack extension value. Additionally, E1820 was designed for metals and brittle ceramics, not flexible composites made of silicone. Thus, the cement-silicone beams were able to continue to bear load long after the standard's failure point, until the last HCP layer had cracked. This extended the plastic region of the cement-silicone beam considerably, so it was at this point that the K_{jc} value was taken. Note that pairwise t-tests between each group of samples showed the K_{ic} values to be statistically significant

at $p < 0.05$, while a pairwise t-test between the K_{jc} values of the solid and cement-silicone samples had $p = 0.22$.

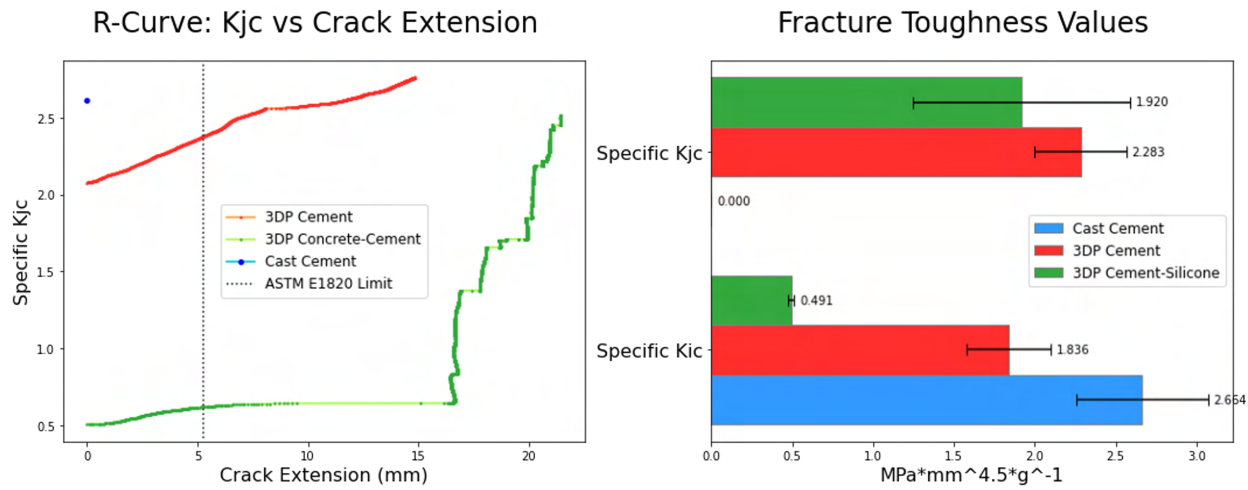


Figure 27: The R-curves for the notched samples (left) and their fracture toughness values (right).

Figure 27 above shows that the solid samples in some cases might have a higher K_{jc} than the cement-silicone ones despite the much larger plastic region of the composite. This is due to the fact that the calculation of K_{jc} involves taking a cumulative sum of the area under the load-displacement curve *starting at the peak load and adding onto K_{ic}* . Thus, the solid samples had a much higher starting point due to their higher peak load and higher K_{ic} values. If this initial K_{ic} is taken as an offset, however, then one can see that the post-peak contribution to the plastic region of the cement-silicone samples, or their net K_{jc} , is much higher ($p = 0.052$, pairwise t-test) than that of the solid samples. This is due to the multiple post-initial-load peaks and the amount of crosshead displacement and CMOD the cement-silicone samples were able to experience before the final HCP layer fractured. This increase in the net fracture toughness of each sample is illustrated below in Figure 28.

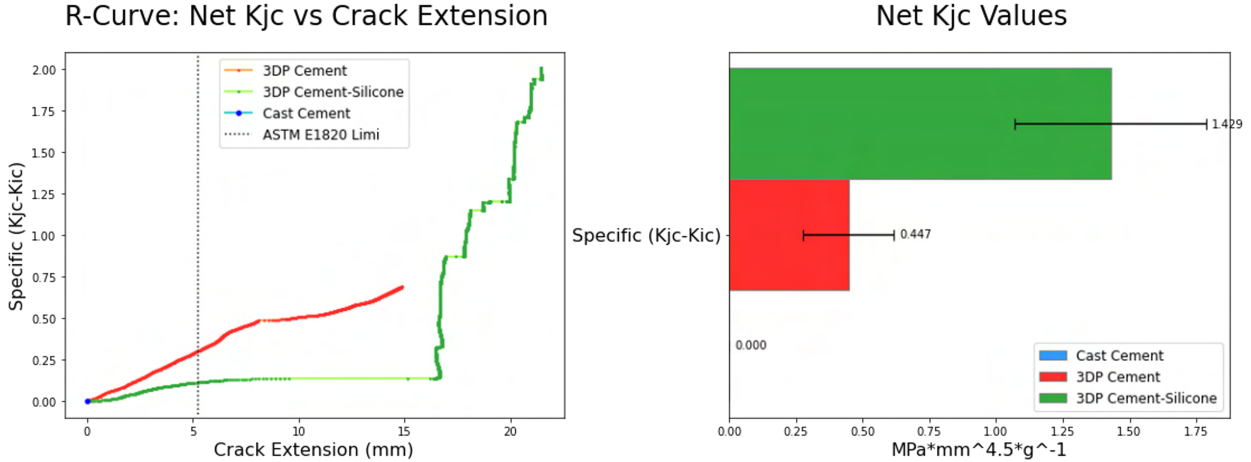


Figure 28: The Offset R-curves for the notched samples (left) and their net fracture toughness values (right).

3.3 Three-Point-Bending Test

The purpose of this test was to validate the cement-polymer rebar concept architecture. Three rebar samples were again compared to three cast and solid samples, with the cement-silicone layered beam being compared as well for completion. The analysis for these tests was much simpler than for fracture toughness, with the peak load being used to calculate MOR according to ASTM C78 and the area under the stress-displacement curve being used to calculate overall toughness. Below in Figure 29 is the specific load-displacement curve of a representative sample of each type after preprocessing.

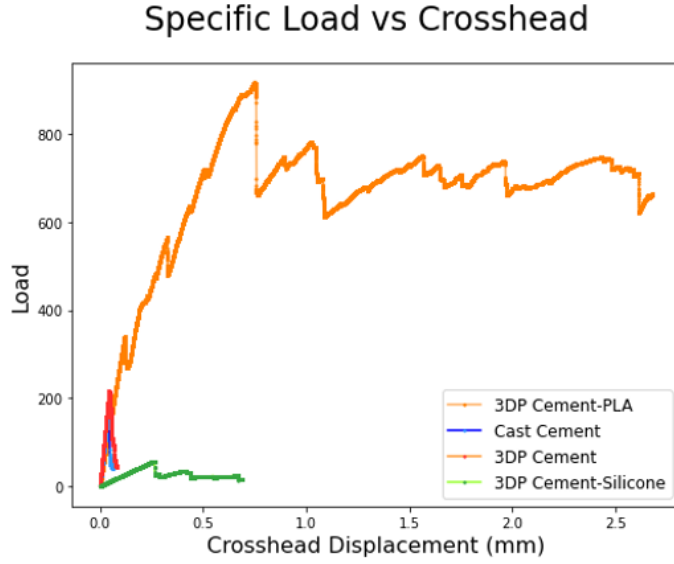


Figure 29: The specific load-displacement curve for each sample type.

The PLA rebars increased the performance of the HCP beam significantly; an impressive result given they made up less than 5% of the beam by mass. They also allowed for a much greater extension of the crosshead, even more so than the cement-silicone beam, as was shown in Figure 25. This was due to the high tensile strength of the PLA (2.3 GPa, about a ten times that of HCP paste) and the way in which the HCP fractured. The rebars held the HCP in place as it cracked, allowing it to continue to act in compression while the rebars took on the tensile stresses from the bottom of the component. This can be seen in the multiple peaks of around the same magnitude in Figure 29, as new cracks formed while the previously-fractured pieces continued to be held in place. This continued until the HCP stopped cracking and all of the load was transferred to the underlying rebars, at which point the load plateaued and the test was stopped. The cracks primarily originated around the ribs of the rebar due to local tensile stress concentrations present in those areas, and were concentrated at the top of the beam around the crosshead. In two out of the three tests, a large section of HCP also broke off from the rest of the beam midway through the test. This crack sequence can be seen below in Figure 30.

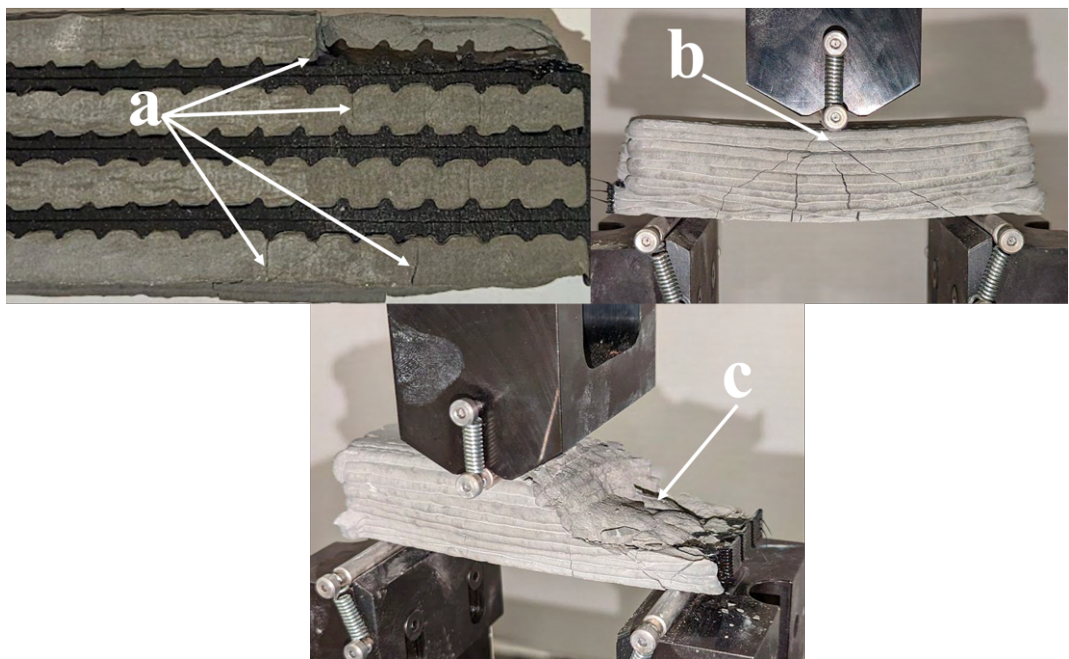


Figure 30: The crack/fracture sequence that took place during each cement-polymer 3PB test: a. crack origins at rebar barbs; b. crack concentrations at crosshead; c. HCP sections breaking off mid-test.

These high peak loads and long post-peak softening resulted in very high MOR and overall toughness values for the cement-polymer components, far outperforming the other beams. Pairwise t-tests between the MORs and overall toughness of the cement-polymer beam and the other three types were statistically significant to a p-value of less than 0.05. Figure 31 describes this in more detail:

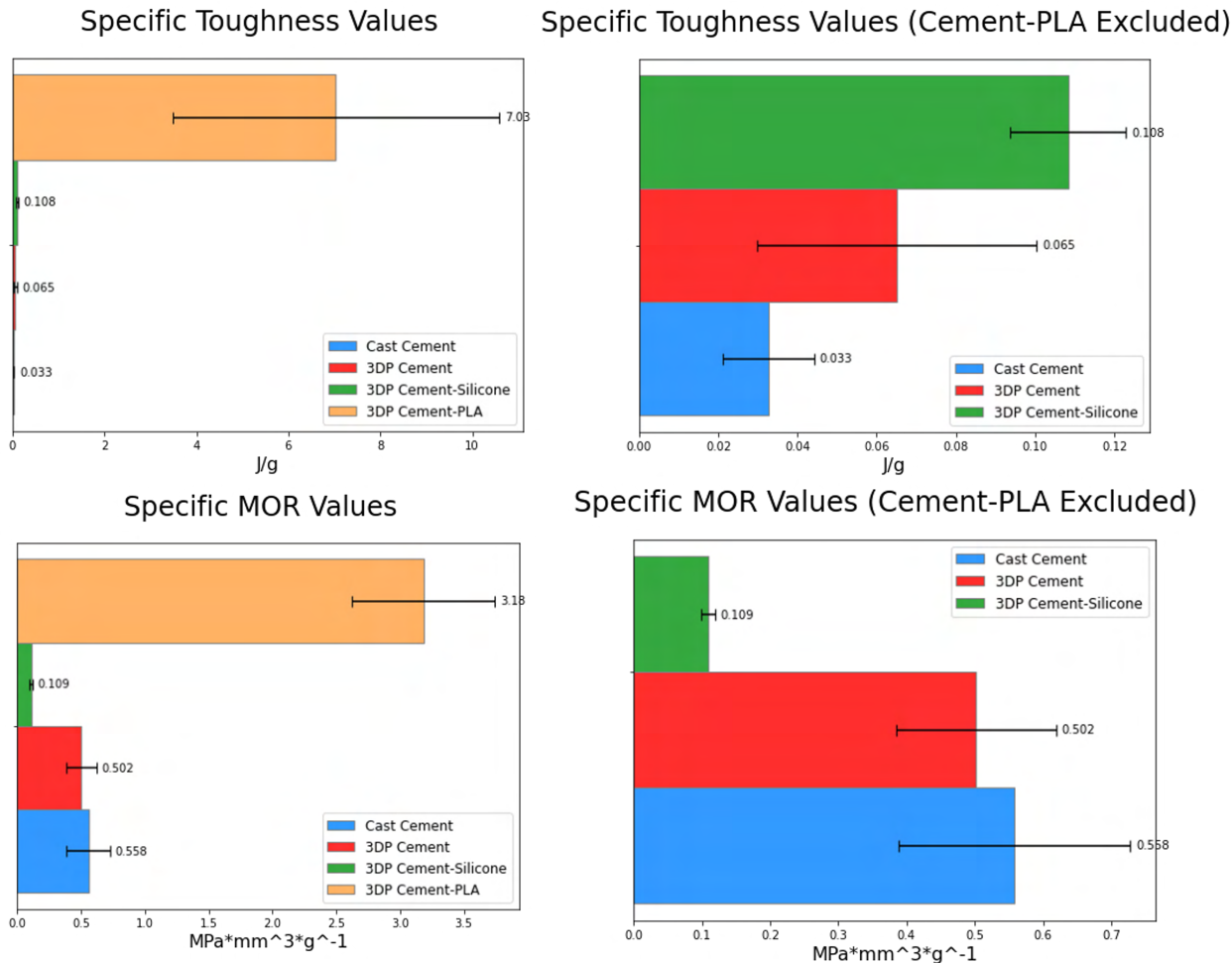


Figure 31: The specific toughness and MOR values for each category of samples. The left column shows all four types, while the left excludes the cement-polymer sample for better viewing of the relative scale of the other three.

A final note of interest is that, the cement-silicone components had improved overall toughness over the cast ($p<0.05$ from pairwise t-test) and solid beams ($p=0.077$ from pairwise t-test) despite their much higher peak loads and specific MORs. Just like was the case with the fracture toughness and with the cement-polymer component, this was due to the much larger post-peak plastic region which contributed much more to the overall toughness than peak loads, and was an impressive result.

4 Conclusion

The purpose of this work was to advance the field of concrete 3D-printing by developing a process for automatically combining concrete with other materials in situ to the printing process. A desktop-scale device capable of combining cement paste with other materials was developed as well as an accompanying toolpath generation workflow. Once the device and its associated control paradigm had been developed sufficiently, it was used for an initial investigation into the creation of multi-material architected materials using cement-polymer and cement-silicone combinations. Each multi-material architecture was printed into a beam shape, allowing for it to be tested on a 3PB testing machine and compared against traditionally cast and 3D-printed single-material components using established ASTM standards.

The cement-polymer beam performed exceptionally well, with the added tensile strength of the PLA components significantly improving its specific MOR and overall toughness. This was done while reducing the component's density and weight compared to a beam made fully of cement paste using a process that allowed two thermally-incompatible materials to be printed alongside each other. This was achievable that due to the fact that on a properly-prepared surface, PLA can be printed without a heated bed and can be rapidly cooled within seconds of being extruded with the use of a cooling fan. This, coupled with the 30-45 seconds needed to complete a tool change, ensured that cement paste was able to be deposited alongside the PLA without concern for any heated components evaporating the water from the uncured cement paste, weakening it. The ribbed rebar design of the polymer component also proved to work very well, providing excellent mechanical bonding between the two materials. The rebar was able to hold the cement in place even as it cracked and fractured during the 3PB test, allowing the plastic deformation region to be significantly extended, making for high amounts of deformation while increasing the multi-material component's tensile strength. In the future, it would be interesting to expand upon this concept, experimenting with different designs of polymer rebar, different mechanical embedding designs, and even different types of reinforcement geometries such as lattice structures.

The cement-silicone beam also demonstrated interesting results. While the thin, spaced-out layers of HCP significantly reduced the overall strength and MOR of the compo-

ment, the flexibility of interlaced silicone layers allowed the beam as a whole to deform much further than was possible for a single-material HCP component before all the cement paste layers were fully cracked. Additionally, even when each HCP layer had been cracked, the bonding between the cement and silicone was enough to keep the component held together and continue to resist the load. This allowed for the post-peak net crack propagation fracture toughness (i.e. net K_{jc}) to be higher than that of the single-material HCP beams. This architected material holds promise, and there is much opportunity for future experimentation. It would be interesting to investigate how little silicone could be used, increasing the component's MOR while still improving its fracture toughness. Additionally, this architecture could be combined with the polymer rebar specimen, resulting in a tri-material component that could leverage the increased strength of the reinforcement with the increased fracture toughness of the cement-silicone layering.

In summary, this work allowed for the creation and automation of (i) a new architected multi-materials in the form of the cement-silicone component, (ii) a new reinforcement strategies in the form of the cement-polymer rebar design, and (iii) novel automated material-specific processing techniques in the form of the tool-changing 3D-printer and its toolpath generation workflow. While the goals set out were achieved, this work still just represented an initial exploration of multi-material concrete 3D-printing, and there are many other directions to take this work, both at the desktop and large scale.

The most immediate improvement to make to the current system would be to modify the cement paste itself. Throughout this work, extrudability issues were rampant, with frequent clogging resulting in failed prints. Thus, a mix design was used that improved extrudability but significantly impacted buildability. Clogging was addressed by tuning the mix design, but this resulted in the material experiencing early-age deformation as subsequent layers were deposited on top, resulting in a trapezoidal cross section for many of the beams and high dimensional variability even as the printer followed identical toolpaths. Moving forward, additional effort must be contributed to further optimizing the cement paste mix design for the nozzle size of the syringe and the specific rheological conditions present within the syringe. Increased dimensional accuracy would significantly improve the quality of the components, as well as allowing for more complex geometries to be printed. Adapting

the syringes to a smaller nozzle size, and tuning the cement paste to avoid flocculation and clogging would also allow for this.

Developing a proper way to start and stop cement paste extrusion within a layer without clogging would also allow the achievable geometries to increase in complexity drastically. Currently, once the prime sequence has been completed at the start of a cement paste layer, that layer must consist of a continuously-connected line of extrusion, as any sort of pausing or retraction will require an additional priming sequence. Developing this system would require a combination of mechanical and cement paste mix design work, and allow the cement paste extrusion to approach the level of freedom that can be obtained from polymer extrusion.

A more automated toolpath generation software would also go a long way. While the current FullControl-RRF-based workflow is extremely powerful, designing a toolpath is still a very manual process that requires deep knowledge of the printer geometry, G-code, and the material characteristics. A Python-based tool capable of function-based, building-block features that are parameterizeable would significantly improve the flexibility of the toolpath design process, allowing for more complex gemoetries to be generated more quickly. The simple addition of a built-in visualizer of the output toolpath would also be immensely helpful in quickly informing the user about the state of their design.

Within the realm of multi-material 3D-printing as a whole, there are any number of directions that are worth exploring. At the desktop scale, increasing the number of materials involved in a multi-material design would be a logical first step. Subtractive tools could be used as well, such as a CNC mill to more precisely shape the polymer or a sculpting tool to shape or texturize the uncured cement paste. Other materials could be explored, including other ceramics and other extrudable silicones or resins. At the large scale, the cement paste syringe could be replaced by a continuously-fed hose, with cement, water, and an accelerant combined at the nozzle to allow for much larger volumes of cement to be printed at a time [32]. In terms of reinforcement, the polymer filament could instead consist of a recycled material, reducing the environmental impact of printing large amounts of polymer, or steel wire could be continuously deployed within the cement paste or concrete extrusion itself [33].

Despite these shortcomings, there is great potential for multi-material concrete 3D-Printing. This work has shown that this technology has the potential to be very impactful,

and warrants additional research.

Appendix A Engineering and Industrial Standards

The independent project described in this thesis incorporated the following engineering and industrial standards:

- Standardized modeling conventions

- Standardized CAD conventions: Autodesk Fusion360 software (standardized file format ISO/ASTM 52915:2013)

To modify the tool-changing platform, Autodesk Fusion360 modeling software was used to generate STL files that were 3D-printed and added to the machine.

- International Units of physical quantities

- International System of Units (SI)

SI units were used throughout the thesis.

- Programming languages and programming practices

- G-code (ISO 6983)

- Python (de-facto standardized)

G-code was used to create toolpaths for the 3D-printer to follow and Python was used to perform data analysis and generate plots.

- Communication (hardware, protocols, and algorithms)

- Buses and protocols: Ethernet (ISO/IEC/IEEE 8802-3:2014)

Ethernet was used to communicate with the Duet 2 control board of the 3D-printer, which was interfaced via a web server hosted on the control board.

- Other

- ASTM standards E1820, E399, C78, C31

Samples were dimensioned, prepared, and tested according to ASTM standards.

References

- [1] Yi Wei Daniel Tay et al. “3D printing trends in building and construction industry: a review”. In: *Virtual and Physical Prototyping* 12.3 (May 2017), pp. 261–276. DOI: 10.1080/17452759.2017.1326724. URL: <https://doi.org/10.1080/17452759.2017.1326724>.
- [2] Mohamadreza Moini et al. “Additive Manufacturing and Performance of Architectured Cement-Based Materials”. In: *Advanced Materials* 30.43 (Aug. 2018), p. 1802123. DOI: 10.1002/adma.201802123. URL: <https://doi.org/10.1002/adma.201802123>.
- [3] Steven J. Schuldt et al. “A systematic review and analysis of the viability of 3D-printed construction in remote environments”. In: *Automation in Construction* 125 (May 2021), p. 103642. DOI: 10.1016/j.autcon.2021.103642. URL: <https://doi.org/10.1016/j.autcon.2021.103642>.
- [4] Izabela Hager, Anna Golonka, and Roman Putanowicz. “3D Printing of Buildings and Building Components as the Future of Sustainable Construction?” In: *Procedia Engineering* 151 (2016), pp. 292–299. DOI: 10.1016/j.proeng.2016.07.357. URL: <https://doi.org/10.1016/j.proeng.2016.07.357>.
- [5] Jingchuan Zhang et al. “A review of the current progress and application of 3D printed concrete”. In: *Composites Part A: Applied Science and Manufacturing* 125 (Oct. 2019), p. 105533. DOI: 10.1016/j.compositesa.2019.105533. URL: <https://doi.org/10.1016/j.compositesa.2019.105533>.
- [6] Freek Bos et al. “Additive manufacturing of concrete in construction: potentials and challenges of 3D concrete printing”. In: *Virtual and Physical Prototyping* 11.3 (July 2016), pp. 209–225. DOI: 10.1080/17452759.2016.1209867. URL: <https://doi.org/10.1080/17452759.2016.1209867>.
- [7] S. El-Sayegh, L. Romdhane, and S. Manjikian. “A critical review of 3D printing in construction: benefits, challenges, and risks”. In: *Archives of Civil and Mechanical Engineering* 20.2 (Mar. 2020). DOI: 10.1007/s43452-020-00038-w. URL: <https://doi.org/10.1007/s43452-020-00038-w>.

- [8] Manu K. Mohan et al. “Extrusion-based concrete 3D printing from a material perspective: A state-of-the-art review”. In: *Cement and Concrete Composites* 115 (Jan. 2021), p. 103855. DOI: 10.1016/j.cemconcomp.2020.103855. URL: <https://doi.org/10.1016/j.cemconcomp.2020.103855>.
- [9] Jianzhuang Xiao et al. “Large-scale 3D printing concrete technology: Current status and future opportunities”. In: *Cement and Concrete Composites* 122 (Sept. 2021), p. 104115. DOI: 10.1016/j.cemconcomp.2021.104115. URL: <https://doi.org/10.1016/j.cemconcomp.2021.104115>.
- [10] A. Perrot et al. “Nailing of Layers: A Promising Way to Reinforce Concrete 3D Printing Structures”. In: *Materials* 13.7 (Mar. 2020), p. 1518. DOI: 10.3390/ma13071518. URL: <https://doi.org/10.3390/ma13071518>.
- [11] Brian Salazar et al. “Polymer lattice-reinforcement for enhancing ductility of concrete”. In: *Materials & Design* 196 (Nov. 2020), p. 109184. DOI: 10.1016/j.matdes.2020.109184. URL: <https://doi.org/10.1016/j.matdes.2020.109184>.
- [12] Harald Kloft et al. “Reinforcement strategies for scp3D-concrete-printing/scp”. In: *Civil Engineering Design* 2.4 (Aug. 2020), pp. 131–139. DOI: 10.1002/cend.202000022. URL: <https://doi.org/10.1002/cend.202000022>.
- [13] Jacek Katzer and Tomasz Szatkiewicz. “Properties of concrete elements with 3-D printed formworks which substitute steel reinforcement”. In: *Construction and Building Materials* 210 (June 2019), pp. 157–161. DOI: 10.1016/j.conbuildmat.2019.03.204. URL: <https://doi.org/10.1016/j.conbuildmat.2019.03.204>.
- [14] J. A. Lewis. “Direct Ink Writing of 3D Functional Materials”. In: *Advanced Functional Materials* 16.17 (Nov. 2006), pp. 2193–2204. DOI: 10.1002/adfm.200600434. URL: <https://doi.org/10.1002/adfm.200600434>.
- [15] Babak Zareiyan and Behrokh Khoshnevis. “Interlayer adhesion and strength of structures in Contour Crafting - Effects of aggregate size, extrusion rate, and layer thickness”. In: *Automation in Construction* 81 (Sept. 2017), pp. 112–121. DOI: 10.1016/j.autcon.2017.06.013. URL: <https://doi.org/10.1016/j.autcon.2017.06.013>.

- [16] Daniel Weger, Dirk Lowke, and Christoph Gehlen. “3D printing of concrete structures using the selective binding method—Effect of concrete technology on contour precision and compressive strength”. In: *Proceedings of the 11th fib International PhD Symposium in Civil Engineering, Tokyo, Japan*. 2016, pp. 29–31.
- [17] Jigang Huang, Qin Qin, and Jie Wang. “A Review of Stereolithography: Processes and Systems”. In: *Processes* 8.9 (Sept. 2020), p. 1138. DOI: 10.3390/pr8091138. URL: <https://doi.org/10.3390/pr8091138>.
- [18] “Linking Solids Content and Flow Properties of Mortars to their Three-Dimensional Printing Characteristics”. In: *ACI Materials Journal* 118.6 (Nov. 2021). DOI: 10.14359/51733136. URL: <https://doi.org/10.14359/51733136>.
- [19] Sunpreet Singh et al. “Current status and future directions of fused filament fabrication”. In: *Journal of Manufacturing Processes* 55 (July 2020), pp. 288–306. DOI: 10.1016/j.jmapro.2020.04.049. URL: <https://doi.org/10.1016/j.jmapro.2020.04.049>.
- [20] *Test Method for Flexural Strength of Concrete (Using Simple Beam with Third-Point Loading)*. DOI: 10.1520/c0078-09. URL: <https://doi.org/10.1520/c0078-09>.
- [21] *Test Method for Measurement of Fracture Toughness*. DOI: 10.1520/e1820-21. URL: <https://doi.org/10.1520/e1820-21>.
- [22] E3D-Online. *ToolChanger and Motion System Bundle*. 2022. URL: <https://e3d-online.com/products/toolchanger-motion-system-bundle> (visited on 09/30/2021).
- [23] E3D-Online. *E3D Hemera Direct Kit (1.75mm)*. 2022. URL: <https://e3d-online.com/collections/hotends/products/e3d-hemera-direct-kit-1-75mm> (visited on 09/30/2021).
- [24] Hyrel3d. *SDS 60*. 2021. URL: <https://www.hyrel3d.com/portfolio/sds-60/> (visited on 09/30/2021).
- [25] Duet3D. *RepRapFirmware 3 overview*. 2022. URL: https://duet3d.dozuki.com/Wiki/RepRapFirmware_3_overview (visited on 09/30/2021).

- [26] ISO. *ISO 6983-1:1982 —Numerical control of machines — Program format and definition of address words — Part 1: Data format for positioning, line motion and contouring control systems*. 2022. URL: <https://www.iso.org/standard/13540.html> (visited on 04/05/2022).
- [27] Andrew Gleadall. “FullControl GCode Designer: Open-source software for unconstrained design in additive manufacturing”. In: *Additive Manufacturing* 46 (Oct. 2021), p. 102109. DOI: 10.1016/j.addma.2021.102109. URL: <https://doi.org/10.1016/j.addma.2021.102109>.
- [28] *Practice for Making and Curing Concrete Test Specimens in the Field*. DOI: 10.1520/c0031_c0031m-19. URL: https://doi.org/10.1520/c0031_c0031m-19.
- [29] Mohamadreza Moini. “Buildability and Mechanical Performance of Architectured Cement-Based Materials Fabricated Using a Direct-Ink-Writing Process”. PhD thesis. Purdue University Graduate School, 2020.
- [30] *Test Method for Linear-Elastic Plane-Strain Fracture Toughness of Metallic Materials*. DOI: 10.1520/e0399-20a. URL: <https://doi.org/10.1520/e0399-20a>.
- [31] Florian Bouville et al. “Strong, tough and stiff bioinspired ceramics from brittle constituents”. In: *Nature Materials* 13.5 (Mar. 2014), pp. 508–514. DOI: 10.1038/nmat3915. URL: <https://doi.org/10.1038/nmat3915>.
- [32] V. Esnault et al. “Experience in Online Modification of Rheology and Strength Acquisition of 3D Printable Mortars”. In: *RILEM Bookseries*. Springer International Publishing, Aug. 2018, pp. 24–38. DOI: 10.1007/978-3-319-99519-9_3. URL: https://doi.org/10.1007/978-3-319-99519-9_3.
- [33] Freek Bos et al. “Experimental Exploration of Metal Cable as Reinforcement in 3D Printed Concrete”. In: *Materials* 10.11 (Nov. 2017), p. 1314. DOI: 10.3390/ma10111314. URL: <https://doi.org/10.3390/ma10111314>.